CrossMark

Effects of Roof-Edge Roughness on Air Temperature and Pollutant Concentration in Urban Canyons

Amir A. Aliabadi[1] · E. Scott Krayenhoff[2] · Negin Nazarian[3] ·
Lup Wai Chew[1] · Peter R. Armstrong[4] · Afshin Afshari[4] ·
Leslie K. Norford[1]

Abstract The influence of roof-edge roughness elements on airflow, heat transfer, and street-level pollutant transport inside and above a two-dimensional urban canyon is analyzed using an urban energy balance model coupled to a large-eddy simulation model. Simulations are performed for cold (early morning) and hot (mid afternoon) periods during the hottest month of the year (August) for the climate of Abu Dhabi, United Arab Emirates. The analysis suggests that early in the morning, and when the tallest roughness elements are implemented, the temperature above the street level increases on average by 0.5 K, while the pollutant concentration decreases by 2% of the street-level concentration. For the same conditions in mid afternoon, the temperature decreases conservatively by 1 K, while the pollutant concentration increases by 7% of the street-level concentration. As a passive or active architectural solution, the roof roughness element shows promise for improving thermal comfort and air quality in the canyon for specific times, but this should be further verified experimentally. The results also warrant a closer look at the effects of mid-range roughness elements in the urban morphology on atmospheric dynamics so as to improve parametrizations in mesoscale modelling.

Keywords Energy balance model · Large-eddy simulation · Mid-range roughness element · Urban canyon · Urban micro-climatology

✉ Amir A. Aliabadi
aliabadi@aaa-scientists.com

[1] Building Technology Program, Department of Architecture, Massachusetts Institute of Technology (MIT), Cambridge, MA, USA

[2] School of Geographical Sciences and Urban Planning, Arizona State University, Tempe, AZ, USA

[3] Singapore-MIT Alliance for Research and Technology Centre, Singapore, Singapore

[4] Masdar Institute of Science and Technology, Abu Dhabi, United Arab Emirates

1 Introduction

The lower portion of the boundary layer over a rough surface is characterized by the surface layer, which can be subdivided into an inertial sublayer and a roughness sublayer (Raupach et al. 1980). Among other factors, the physical properties of the urban canopy determine the magnitude and direction of momentum, energy, and pollutant exchanges between the roughness sublayer and the inertial sublayer, and ultimately the mixed layer (or the urban boundary layer above). Such parameters include the geometrical characteristics [building height, plan area density (λ_p), and frontal area density (λ_f)], material and aerodynamic properties (radiation properties of building facets and roughness of building facets), and energy and pollutant exchange characteristics (anthropogenic generation of heat and pollutants in indoor and outdoor spaces and thermal mass of buildings).

Various experimental and numerical studies have been conducted to understand such exchanges, either with the goal of developing design solutions or analysis tools to predict outdoor temperatures, pollutant dispersion, and airflow patterns, or with the aim of developing models for coupling with mesoscale weather forecasting or air quality models. For example, multiple wind-tunnel and water-channel experiments have been conducted to improve the understanding of airflow and heat transfer among cube-like elements, representing buildings at reduced scale (Uehara et al. 2000; Cheng and Castro 2002; Li et al. 2008). Various full-scale field campaigns have also been conducted to monitor physical quantities such as air temperature, humidity, velocity vector, and the turbulent fluxes of momentum and heat (Nakamura and Oke 1988; Louka et al. 2000; Rotach et al. 2005; Roulet et al. 2005; Eliasson et al. 2006; Klein and Clark 2007; Inagaki and Kanda 2008; Masson et al. 2008; Christen et al. 2009; Balogun et al. 2010; Blackman et al. 2015; Klein and Galvez 2015). These full-scale experiments are particularly useful for model validation. A variety of single-layer urban energy balance models, based on an aerodynamic resistance parametrization, have been developed that enable the prediction of the flow velocity vector and temperature within urban canyons (Masson 2000; Kusaka et al. 2001; Krayenhoff and Voogt 2007; Bueno et al. 2012). With the application of computational fluid dynamics (CFD), prognostic one-dimensional turbulent diffusion models have been developed to predict the velocity vector and temperature within the urban roughness sublayer (Martilli and Santiago 2007; Santiago and Martilli 2010; Santiago et al. 2013; Krayenhoff et al. 2015). Advances in one-dimensional turbulent diffusion models have made possible the development of multi-layer urban energy balance models to complement single-layer models for some applications, either as stand-alone analysis tools, or as sub-modules to be coupled to mesoscale atmospheric models (Martilli et al. 2002; Hamdi and Masson 2008; Krpo et al. 2010; Krayenhoff et al. 2015). In addition, various three-dimensional CFD models have been used to clarify detailed processes in pollutant dispersion, heat transfer, and airflow within the urban roughness sublayer (Coceal et al. 2006; Santiago et al. 2007, 2014; Li et al. 2010, 2012; Flores et al. 2013; Yuan et al. 2014; Giometto et al. 2016; Goodfriend et al. 2016; Nazarian and Kleissl 2016).

In virtually all modelling efforts, however, the urban geometry or morphology has been approximated without accounting for the effects of mid-range roughness elements including balconies, air conditioning equipment on the roofs or walls, facet extensions, people, and vehicles. For the simplest analyses, the urban morphology is modelled with a single roughness length, itself parametrized as a function of average building height. For more advanced analyses, repeatable block units, or a group of blocks with different heights, are used where other parameters such as plan area density (λ_p), frontal area density (λ_f), and the roughness length of building facets are introduced. Overall, the available literature addresses urban

characteristic lengths in the range of 10–1000 m, so mid-range length scales under 10 m are generally excluded (Arnfield 2003; Vardoulakis et al. 2003). In a very limited number of studies, the effects of slanted roof shapes or equipment on the roofs are considered in pollutant transport within the urban environment (Rafailidis 1997; Kastner-Klein et al. 2004; Huang et al. 2009, 2015; Saathoff et al. 2009; Yassin 2011; Takano and Moonen 2013). However, it remains to be seen whether mid-range roughness elements, i.e. those with characteristic sizes larger than 0.1 m but smaller than building characteristic lengths (<10 m), play a significant role in the exchanges of momentum, energy, and pollutants within the urban roughness sublayer as well as the remainder of the atmospheric boundary layer.

There are two benefits in understanding the effects of mid-range roughness elements on the exchanges of momentum, energy, and pollutants within the urban roughness sublayer. First, unique case-driven engineered solutions can be methodically tested and tailored to control temperature, air quality, and airflow within urban canyons. Second, urban effects can be parametrized more reliably within mesoscale modelling frameworks. This latter benefit may result in improvements in predictions by urban climate models that, to our knowledge, has not previously been investigated rigorously.

1.1 Objectives

We investigate the effect of a roof fence, as a mid-range roughness element, on the airflow, temperature, and pollutant concentration in urban canyons in a hot climate using a case study in Abu Dhabi, United Arab Emirates. The roof fence is assumed as a solid and non-porous barrier, and it is considered to be a thermally passive element with zero convective, conductive, and radiative heat transfer with the surroundings (i.e. zero heat flux). The analysis is limited to a two-dimensional urban canyon oriented north-south with unit aspect ratio and near-perpendicular wind directions, i.e. wind directions that make at least about a 30-degree angle with the street axis according to the classifications of Vardoulakis et al. (2003). The roof fence is a vertical element of size 5–20% of the building height, which is installed on one edge of a roof. All meteorological conditions considered are those monitored at the site for the hottest month (August) of the year 2010. The sensitivities of the velocity vector, temperature, and pollutant dispersion (pollutant released from the street level) in the urban canyon and aloft are studied as functions of high and low surface temperatures (in the diurnal cycle) and the height of the roughness element.

Variations of thermal and radiative parameters in the energy balance model, such as volumetric heat capacity, surface albedos and emissivities, have been addressed extensively in the literature and are not the focus of the present study. For example, increasing the roof albedo by 0.6 has been shown to reduce the urban-canyon temperature by more than 1 K (Krayenhoff and Voogt 2010).

2 Methodology

The methodology involves a four-step process. First, meteorological conditions that were monitored at the site during the entire year of 2010 are analyzed to determine a subset of forcing conditions for an energy balance model and a CFD model. Second, the energy balance model is used to derive facet temperatures of an urban canyon at 1-h resolution given the forcing meteorological dataset for generic design parameters. These parameters include day of the year, building construction material thicknesses, thermal conductivities, volumetric heat capacities, surface albedos, emissivities, canyon-aspect ratio, street orientation, and cloud

Fig. 1 Meteorological mast in Masdar city

type. Third, a CFD model is developed and validated against wind-tunnel measurements. Fourth, using one-way coupling, the meteorological conditions and facet temperatures from the energy balance model are used as boundary conditions for a limited number of CFD model simulations. This is used to investigate the effects of roof-mounted mid-range roughness elements (fences) on airflow, heat transfer, and pollutant dispersion processes within and above the urban canyon. A limited number of two-way coupled simulations, between the energy balance and CFD models, are also performed to quantify potential errors associated with one-way coupling.

2.1 Meteorological Context in Abu Dhabi

Meteorological conditions at Abu Dhabi are analyzed using hourly measurements of air temperature, wind speed, and wind direction at heights of 3 and 10 m above the ground, respectively, in 2010. The station used for data collection was a 10-m mast located at 24.420050°N and 54.612718°E in Masdar city (Fig. 1). Most measurements were made using a Campbell Scientific model CS215 based on Sensirion's CMOSens technology for temperature measurement with accuracy of $\pm 0.4°C$ ($\pm 0.9°C$ for temperature $>40°C$), an NRG Systems model RNRG 40C 3-cup anemometer for wind-speed measurement with accuracy of $\pm 0.1\,\mathrm{m\,s^{-1}}$ (within $5–25\,\mathrm{m\,s^{-1}}$), and an NRG Systems model RNRG 200P direction vane for wind-direction measurement. The city faces the Persian Gulf in the north-west direction, and temperature minima and maxima occurred in January (low) and August (high), respectively. Wind-speed variations were consistent, with low wind speeds at night and peak wind speeds in mid afternoon. Furthermore, a consistent diurnal variation in wind direction is identified, indicating the presence of a significant sea breeze in mid afternoon.
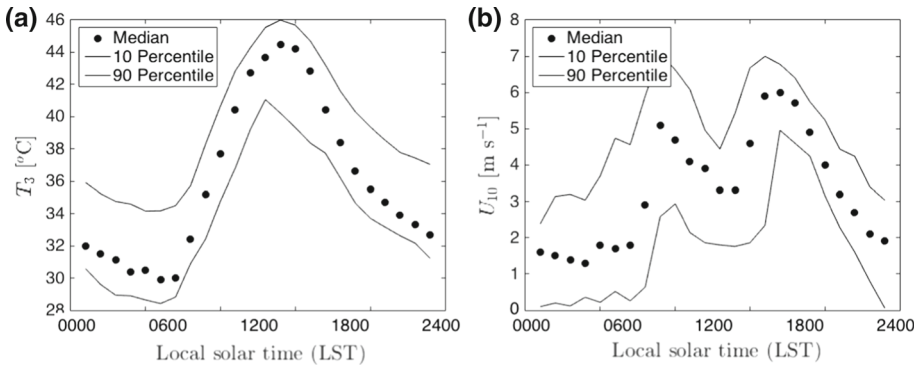
Fig. 2 Statistical quantiles for meteorological measurements in August 2010: **a** temperature (T_3), **b** wind speed (U_{10})

Figure 2 shows statistical quantiles (10th percentile, median, and 90th percentile) for hourly-resolved meteorological variables in the month of August. The 10th and 90th percentiles are chosen as statistical estimators representing the spread in the data distribution. This statistical range suggests a predictable diurnal cycle for temperature, wind speed, and relative humidity (not shown), with the median values taken as representative, and used for analysis in the subsequent simulations. For this analysis, wind speeds are extrapolated to 30-m height using the logarithmic profile. The temperature values are not extrapolated since, at heights of interest, typical lapse rates do not result in significant vertical temperature variations over flat terrain.

Since Masdar city is not yet fully developed, the meteorological measurements do not represent all of the urban effects precisely, particularly the urban heat-island effect. However, since our study is framed as a sensitivity test, to predict the influence of roof roughness elements on *changes* in temperature and pollutant concentration inside and above the canyon, our predictions are justified and can be understood on the *relative* scale, if not the *absolute* scale.

2.2 Energy Balance Model

The energy balance model adopted is the Temperature of Urban Facets 3D (TUF-3D) model developed by Krayenhoff and Voogt (2007), which is a dry, three-dimensional microscale urban energy balance model with a focus on radiative exchange. In this model, plane-parallel facets, including roofs, walls, and streets, are decomposed into identical square patches that exchange shortwave and longwave radiation with other patches and with the sky, sensible heat by conduction with underlying building and street material, and sensible heat by convection with the atmosphere, including the canyon air. Six patches in each direction (x, y, and z) for all facets are used. The freestream meteorological measurements discussed in Sect. 2.1 are used to force this model, while the downwelling shortwave and longwave radiation are calculated using the site latitude and the solar angle.

Input parameters to the model for building and street construction material include layer thicknesses, thermal conductivity, and volumetric heat capacity. The TUF-3D model takes input parameters for urban-canyon geometry such as plan area density (λ_p) and building-height to building-width ratio (H/R) and calculates the corresponding building-height to street-width ratio (H/S), also known as the canyon-aspect ratio. The canyon axis is oriented

Table 1 CFD simulation boundary conditions as a function of local solar time (LST); subscripts are as follows: A (upstream), R (roof), S (street), EW (east wall), and WW (west wall)

LST	Wind direction (°)	U_A (m s^{-1})	T_A (°C)	T_R (°C)	$\overline{T_S}$ (°C)	$\overline{T_{EW}}$ (°C)	$\overline{T_{WW}}$ (°C)
0400 LST	114.3	2.19	30.4	23.2	28.8	28.4	28.4
1600 LST	333.9	9.92	42.8	49.9	45.3	42.9	49.1

north-south, and solar angles are calculated given the latitude of the site and day of the year. The model data considered are the spatially- and temporally-resolved facet temperatures. To approximate a two-dimensional canyon, the model temperatures along the centre of the facets (with respect to the spanwise direction) are extracted and used as boundary conditions for the CFD simulations. More details on the TUF-3D model and its validation against field measurements can be found in Krayenhoff and Voogt (2007).

2.3 Computational Fluid Dynamics (CFD)

All reported times are in local solar time (LST). Due to the inherent computational cost of CFD models only two local solar diurnal times corresponding to cold (0400 LST) and hot (1600 LST) periods are chosen for simulations. However, for each time detailed sensitivity tests are performed by varying the height of the roof roughness element according to the following conditions: (a) no fence, (b) $0.05H$, (c) $0.1H$, and (d) $0.2H$ high fences on one side of the roof, where H is the building height. Table 1 shows the boundary conditions for CFD simulation cases.

The open source CFD software used is OpenFOAM 3.0.1. The standard solver adapted is `buoyantBoussinesqPimpleFoam`, which is enabled with the `oneEqEddy` large-eddy simulation (LES) turbulence model and a passive scalar transport model, to be discussed in detail in Sect. 2.3.1 (Greenshields 2015). It is run on parallel mode using 44 central processing units on a Linux platform. LES models have been successfully employed to simulate airflow and heat transfer in the urban environment and are preferred over Reynolds-averaged Navier–Stokes (RANS) or unsteady RANS turbulence models (Nazarian and Kleissl 2016). The one-equation LES model has also been successfully employed to simulate airflow and heat transfer within urban canyons (Li et al. 2008, 2010, 2012).

2.3.1 LES Model

An incompressible turbulent flow based on a one-equation subgrid-scale (SGS) model is considered. The dimensionless Navier–Stokes equations are developed and discussed below using the reference length scale H (the building height of the street canyon), the reference upstream velocity U_A, and the reference upstream temperature T_A. With this model, the continuity equation becomes

$$\frac{\partial \overline{u}_i}{\partial x_i} = 0, \tag{1}$$

where the overbar notation signifies the spatially- and temporally-resolved velocity. Using the Boussinesq approximation the momentum and SGS turbulent kinetic energy (TKE) equations become

$$\frac{\partial \overline{u}_i}{\partial t} + \frac{\partial}{\partial x_j} \overline{u}_i \overline{u}_j = -\frac{\partial \overline{p}}{\partial x_i} - \frac{\partial \tau_{ij}}{\partial x_j} + \frac{1}{Re} \frac{\partial^2 \overline{u}_i}{\partial x_j \partial x_j} + Ri\delta_{i3}, \tag{2}$$

$$\frac{\partial k_{\text{sgs}}}{\partial t} + \overline{u}_i \frac{\partial k_{\text{sgs}}}{\partial x_i} = P + B - \epsilon + \frac{\partial}{\partial x_i} \left(\frac{2}{Re_{\text{T}}} \frac{\partial k_{\text{sgs}}}{\partial x_i} \right), \tag{3}$$

where $\overline{u}$ is the spatially- and temporally-resolved velocity, k_{sgs} is SGS TKE, $Re = U_A H/\nu$ is the Reynolds number, $Ri = gH\overline{T}/U_A^2$ is the Richardson number, and $Re_{\text{T}} = U_A H/\nu_{\text{T}}$ is the turbulent Reynolds number (Li et al. 2010). The symbol $\overline{p}$ denotes the resolved-scale modified pressure, normalized by constant density

$$\overline{p} = \overline{p}^* + \frac{1}{3}\tau_{ii}, \tag{4}$$

where $\overline{p}^*$ is the resolved-scale static pressure. Other quantities in the above equations are as follows

$$\tau_{ij} = \overline{u_i u_j} - \overline{u}_i \overline{u}_j, \tag{5}$$

$$P = -\tau_{ij}\overline{S}_{ij}, \tag{6}$$

$$B = -g\nu_\theta \frac{\partial \overline{T}}{\partial z}, \tag{7}$$

$$\epsilon = C_\epsilon \frac{k_{\text{sgs}}^{3/2}}{l}, \tag{8}$$

where τ_{ij} is the SGS momentum flux, P is the shear production, B is the buoyant production, and ϵ is the dissipation rate. The new terms in these equations require further parametrization using

$$\overline{S}_{ij} = \frac{1}{2} \left(\frac{\partial \overline{u}_i}{\partial x_j} + \frac{\partial \overline{u}_j}{\partial x_i} \right), \tag{9}$$

$$\nu_{\text{T}} = C_k k_{\text{sgs}}^{1/2} l, \tag{10}$$

$$\nu_\theta = \frac{\nu_{\text{T}}}{Pr_{\text{T}}}. \tag{11}$$

The turbulence model is closed by using parametrizations for the remaining quantities. The turbulent Prandtl number (Pr_{T}) is taken to be 0.85 (Rotta 1964; Reynolds 1975; Flores et al. 2013), C_k is taken to be 0.094, and C_ϵ is taken to be 1.048. The length scale ($l = (\Delta x \Delta y \Delta z)^{1/3}$) is estimated as a function of local grid size but damped near the walls using van Driest damping functions to prevent excessive dissipation of TKE near the walls (van Driest 1956). The SGS momentum flux is parametrized using the eddy-viscosity assumption,

$$\tau_{ij} = -2\nu_{\text{T}}\overline{S}_{ij}. \tag{12}$$

The energy equation for the spatially- and temporally-resolved temperature ($\overline{T}$) in the LES model is provided below and is closed by parametrizing the SGS heat flux using the eddy-conductivity assumption,

$$\frac{\partial \overline{T}}{\partial t} + \frac{\partial}{\partial x_i} \overline{u}_i \overline{T} = -\frac{\pi_i}{\partial x_i} + \frac{1}{Re Pr} \frac{\partial^2 \overline{T}}{\partial x_i \partial x_i}, \tag{13}$$

$$\pi_i = \overline{u_i T} - \overline{u}_i \overline{T} = -\nu_\theta \frac{\partial \overline{T}}{\partial x_i}, \tag{14}$$

where the laminar Prandtl number (Pr) for air is assumed to be 0.7. Finally, the transport equation for the spatially- and temporally-resolved passive scalar ($\bar{s}$) in the LES model is formulated and solved accounting for advective transport, SGS transport, and molecular diffusion using

$$\frac{\partial \bar{s}}{\partial t} + \frac{\partial}{\partial x_i} \bar{u}_i \bar{s} = -\frac{\partial \sigma_i}{\partial x_i} + \frac{1}{ReSc} \frac{\partial^2 \bar{s}}{\partial x_i \partial x_i}, \tag{15}$$

where Sc is the Schmidt number. The SGS component of the transport is modelled using the eddy-viscosity assumption,

$$\sigma_i = \overline{u_i s} - \bar{u}_i \bar{s} = -\frac{\nu_T}{Sc_T} \frac{\partial \bar{s}}{\partial x_i}, \tag{16}$$

where Sc_T is the turbulent Schmidt number. Since for air the Lewis number $Le = Sc/Pr \approx 1$, we can employ the concept of Reynolds analogy and assume $Pr = Sc$ and $Pr_T = Sc_T$ (Reynolds 1975; Flores et al. 2013).

2.3.2 Finite Volume Schemes

A second-order implicit backward time scheme is used, and all gradient schemes are based on second-order Gaussian integration with linear interpolation. All Laplacian schemes are based on corrected Gaussian integration with linear interpolation, which provides an unbounded, second-order, and conservative numerical behaviour. Divergence schemes are based on Gaussian integration with linear or upwind interpolation, depending on the variable of interest (Greenshields 2015).

2.3.3 Finite Volume Solution Control

Throughout all simulations, timesteps are chosen so that the maximum Courant number ($Co = \delta t |U|/\delta x$) for all cells within the computational domain stays below one. The pressure matrix is preconditioned by the diagonal incomplete Cholesky technique and solved by the preconditioned conjugate gradient solver. Other variables are preconditioned by the diagonal incomplete-lower-upper technique and solved by the preconditioned bi-conjugate gradient solver. The pressure-linked equations (i.e. equations that have a pressure term) are solved by a hybrid method consisting of two algorithms: (1) the pressure-implicit split-operator method, and (2) the semi-implicit method (Greenshields 2015).

2.3.4 Solution Averaging

Once steady conditions for the time-averaged solutions are achieved, the simulations are extended for an additional $1000H/U$ in time to obtain statistical information by time and spatial averaging. The timestep of the simulation is $0.01H/U$, with the choices of simulation time and timestep following the acceptable values used by Li et al. (2010), i.e. $300H/U$ and $0.005H/U$, respectively. The solutions for all variables in the entire domain are averaged at every timestep and saved every $100H/U$ to reduce disk storage requirements. In addition, instantaneous solutions are saved at every timestep in strategic portions of the domain, including vertical lines over the building roofs and in the canyons at various streamwise distances (see Fig. 3), to calculate resolved turbulent and dispersive variances and fluxes.
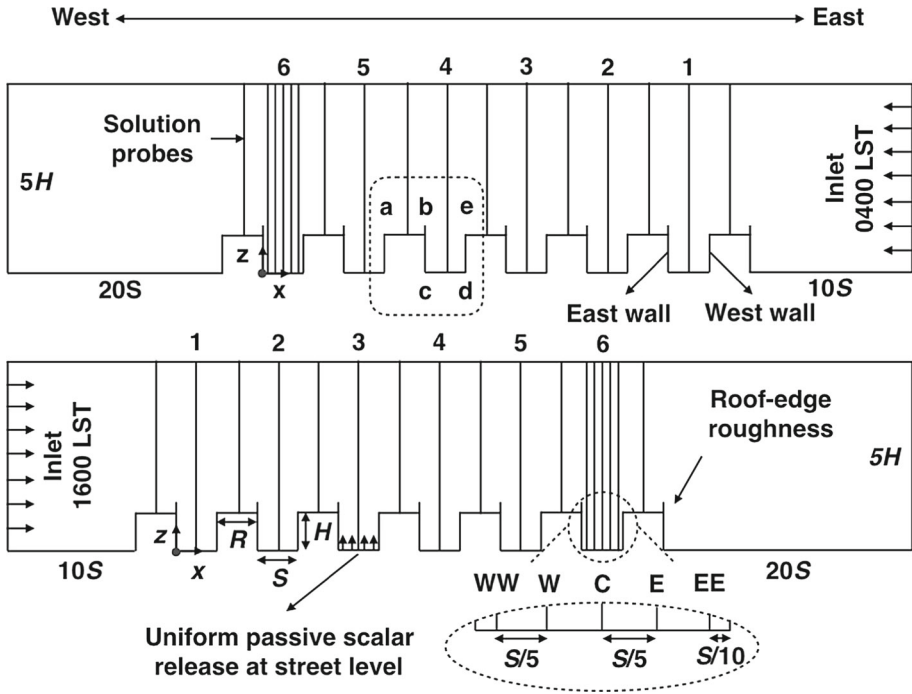
Fig. 3 Numerical domain for the urban-canyon CFD simulations; note that the passive scalar release occurs in all canyons

2.3.5 Geometry and Mesh

The LES model requires realistic turbulent fluctuations at the inlet for successful simulation of the turbulent flow. Such fluctuations must meet several criteria: (a) they must be stochastically varying, on scales down to the spatial and temporal filter scales, (b) be compatible with the Navier–Stokes equations, (c) represent turbulence realistically (i.e. consist of coherent eddies across a range of spatial scales down to the Kolmogorov scale), (d) allow easy specification of turbulent properties, and (e) be easy to implement (Tabor and Baba-Ahmadi 2010). Two common approaches that generate inlet turbulent fluctuations for LES models are the synthetic and precursor methods, where in the former, random fields are constructed at the inlet using Fourier techniques and principle orthogonal decomposition methods, while in the latter a simulation is performed to generate the desired fluctuations. Precursor methods are shown to be more accurate but more computationally demanding and more difficult to implement (Tabor and Baba-Ahmadi 2010).

To implement the synthetic method, a large computational domain is used with street width S, building height H, and roof width R (see Fig. 3). The upstream and downstream distances are $10S$ and $20S$, respectively, with the domain size conservatively larger than that used by Martilli and Santiago (2007) and Santiago et al. (2007). The height of the domain is $5H$. The top of the domain in the CFD model should ideally be positioned above the roughness sublayer, which is often found to be of depth three to five times the height of the main roughness element (i.e. building height or H) (Cheng and Castro 2002). Various values between $2H$ and $6H$ have been used in previous CFD studies, e.g. $2H$ (Li et al. 2010),

$4H$ (Santiago et al. 2014), $4H$ (Coceal et al. 2006), and $6H$ (Nazarian and Kleissl 2016). Five canyons are used upstream of the sixth canyon, for which we report the numerical results. This is guided by a similar choice reported by Martilli and Santiago (2007) and Santiago et al. (2007). The depth of the domain in the spanwise direction is 0.75 times the characteristic length of the geometry $L = \sqrt{SH}$ or H in our case, where $H = S = R = 10$ m. Larger streamwise and spanwise domain sizes are generally desired if one is interested in capturing unsteady large-scale organized structures that develop in three-dimensional canyons (Kanda et al. 2004). However, for the two-dimensional canyon in question, we determined by sensitivity analysis that the domain size in the streamwise and spanwise directions is adequate. The smaller domain size benefits our simulations because the mesh resolution can be increased and a realistic high building Reynolds number, Re_H, as large as $O(10^6)$, can be used.

The mesh resolution required by any LES model is usually restricted by the flow conditions and the geometry. If the viscous sublayer near the walls is to be resolved, the condition $y^+ = u_* y / \nu < 1$ must be satisfied near all walls (Bredberg 2000). Here, u_* is the friction velocity, y is the normal distance from the wall surface to the centre of the adjacent computational cell, and ν is the kinematic viscosity. Alternatively, the use of wall functions, particularly the Launder and Spalding (1974) and Jayatillaka (1969) wall functions that are used herein, permits $30 < y^+ < 200$ and hence greatly reduces computational cost (Efros 2006). The maximum grid size in the domain (Δ_{max}) must satisfy the condition $\Delta_{max} < 0.05L$, as also confirmed by Yaghoobian et al. (2014), where L is the characteristic size of the geometry and at the same time represents the largest eddy size formed in bluff-body flow.

The mesh is created using the `blockMesh` utility provided in OpenFOAM, a tool that generates a structured hexahedral mesh with high control on mesh spacing. A simple grading scheme in `blockMesh` calculates the cell sizes using a simple geometric progression so that along a length l, if n cells are requested with a ratio of $M > 1$ between the last and first cells, then the size of the smallest cell is $\delta x_s = l(r-1)/(Mr-1)$, where $r = M^{\frac{1}{n-1}}$ (Greenshields 2015). Using this progression, mesh sizing is varied in the x and z directions. Using the methodology of White (2003), cell thicknesses adjacent to the surfaces are first estimated and implemented a priori for $30 < y^+ < 200$ (for using wall functions) corresponding to the Re_H of the flow. The y^+ value is then independently checked a posteriori using OpenFOAM's utility `yPlus`, which calculates y^+ along all patches including the walls, street, roof, and fence (Greenshields 2015), to ensure the condition $30 < y^+ < 200$ is met. It is also ensured that $\Delta_{max} < 0.05L$.

The number of control volumes in the spanwise direction, y, is $n_y = 16$, and within each canyon there are $n_x = 20$ by $n_z = 20$ control volumes. Along the building roof there are $n_x = 20$ control volumes, while for the fence, $n_z = 10$ control volumes are used. On top of the fence and up to the top of the domain, $n_z = 48$ control volumes are used. Each canyon and building module contains 45,056 control volumes, with the entire mesh containing 376,788 control volumes.

2.3.6 Boundary Conditions

All spanwise boundary conditions are periodic, while the the top lid boundary condition is zero gradient for all variables. Given the large length of the domain in the streamwise direction, a constant wind-speed profile is used at the inlet, which develops into a vertical profile suitable for the urban roughness sublayer by the time the airflow reaches the sixth canyon (Masson 2000; Kusaka et al. 2001; Harman et al. 2004; Martilli and Santiago 2007;

Santiago et al. 2007). A turbulence intensity $TI = k/(0.5U^2) = 0.05$ is inserted at the inlet, where k is the TKE and U is the mean air speed (Kim and Baik 2003). At the outlet a fixed pressure boundary condition is implemented, and the velocity is switched between fixed value (zero) and zero gradient depending on the direction of the airflow. This boundary condition prevents the air from entering the domain where recirculation zones are to appear at the outlet. A no-slip condition is implemented with respect to the walls, street, roof, and fence.

Given the large length of the domain in the streamwise direction, a constant temperature profile is used at the inlet, which develops into a vertical profile suitable for the urban roughness sublayer by the time the airflow reaches the sixth canyon (Lemonsu et al. 2004; Krayenhoff and Voogt 2007; Martilli and Santiago 2007; Santiago et al. 2007). At the outlet, the temperature is switched between fixed value (ambient) and zero gradient depending on the direction of the airflow. The surface temperatures for the roof, walls, and street are provided by the TUF-3D model, which accounts for the spatial variability due to the sun angle and time of day. When the roof fence is used, the adiabatic or zero-gradient condition for the temperature is implemented at the fence.

For the passive scalar, an arbitrary unitless and uniform value of unity is applied at the street level, representing the anthropogenic pollutants from road vehicles. A zero-gradient condition is applied at the walls, roof, and fence, while at the inlet a fixed value of zero is assigned, and at the outlet, the passive scalar is switched between fixed value (zero) and zero gradient again, depending on the direction of the airflow.

2.4 Justification for One-Way Coupling and Limited Two-Way Coupling Tests

A two-way coupling between the energy balance and CFD models is not considered for all of the simulation cases because of practical limitations.[1] The TUF-3D model timestep (10–100 s) is too coarse compared to the CFD timestep (0.01 s), which makes a two-way coupled model too computationally expensive. The approach for one-way coupling of the energy balance and CFD models may introduce errors in the calculation of the surface temperature and subsequently the canyon air temperature and the pollutant concentration in response to the altered velocity vector field in the domain, which is caused by the implementation of the roof fence. This is expected since the alteration of the velocity vector field changes the convective heat transfer to the building exterior surfaces. The use of one-way coupling, however, can be justified by a sensitivity analysis.

A limited two-way coupling of the CFD and TUF-3D models is performed so as to understand the effects on the temperature and passive scalar concentrations within the computational domain. To do this, first the TUF-3D model is run to supply the temperature boundary conditions to the CFD model. Subsequently, the convective heat transfer coefficients are calculated in the CFD model and the percentage changes in them, due to the addition of the roof fence, are recorded. In one iteration, these changes in the convective heat transfer coefficients are implemented in the TUF-3D model to arrive at a new set of temperature boundary conditions for the CFD model. Lastly, the CFD model is run again with these new surface temperatures, and the difference in the temperatures and the passive scalar concentrations in the CFD model before and after this iteration are analyzed and presented in Sect. 3.3. This sensitivity test bolsters our results by indicating a favourable additional temperature reduction at the hottest time of the day around 1600 LST, justifying the use of the roof fence.

---

[1] The TUF-3D model is developed in Fortran while OpenFOAM is developed in C++.

Fig. 4 Average facet
temperatures predicted by the
TUF-3D model
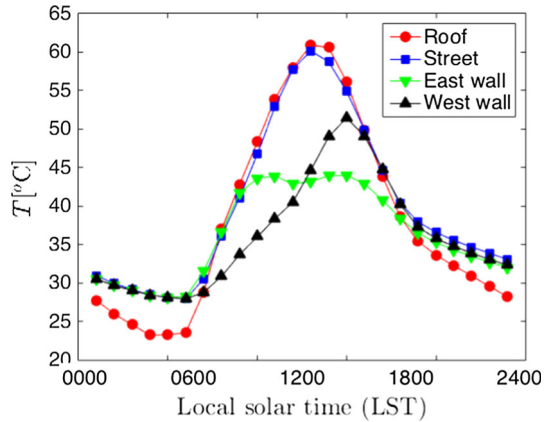
3 Results and Discussion

3.1 TUF-3D Model

The TUF-3D model is run assuming that the model default parameters are used: albedos
for the roof, street, and walls are 0.15, 0.10, and 0.30, respectively, while the corresponding
emissivities are 0.92, 0.92, and 0.88. A clear-sky condition is assumed in this study. Full
conduction between the deepest layer and the ground or the building interior is assumed, and
the internal resistance to energy exchange between the deepest building layers and the building
interior air is taken to be $0.123 \, \mathrm{m^2 \, K \, W^{-1}}$, approximating the combined conductive, radiative,
and convective heat transfer (Masson et al. 2002). Four building layers are considered for the
roof, street, and walls, with the corresponding thicknesses varying in the ranges of 0.01–0.03,
0.02–0.50, and 0.02–0.09 m. Thermal conductivities are in the ranges of 0.03–1.50, 0.30–
0.90, and $0.30–1.10 \, \mathrm{W \, m^{-1} \, K^{-1}}$, respectively, and the volumetric heat capacities are in the
ranges of 0.10–2.25, 1.25–0.20, and $1.50–2.00 \, \mathrm{MJ \, m^{-3} \, K^{-1}}$, respectively. The simulations
also require a set of constants including the initial building internal air temperature ($22°C$)
and the deep ground temperature ($17°C$). Figures 4 and 5 show the average and the spatial
variations in the facet temperatures, where each facet is discretized by six patches along each
surface direction. There is a noticeable time and magnitude shift between the east-wall and
the west-wall temperature peaks that is expected.

3.2 CFD Model

The CFD model is first validated against the wind-tunnel experiments of Uehara et al. (2000),
and the validation is presented in Appendix 1.

3.2.1 Calculation of Turbulent and Dispersive Fluxes and Variances

We use the methodology of Martilli and Santiago (2007) to calculate the turbulent and the
dispersive fluxes and variances at each vertical level, where the total flux or variance is given
as

$$<\overline{ab}> = \underbrace{<\bar{a}><\bar{b}>}_{\mathrm{I}} + \underbrace{<\overline{a'b'}>}_{\mathrm{II}} + \underbrace{<\tilde{a}\tilde{b}>}_{\mathrm{III}}, \tag{17}$$
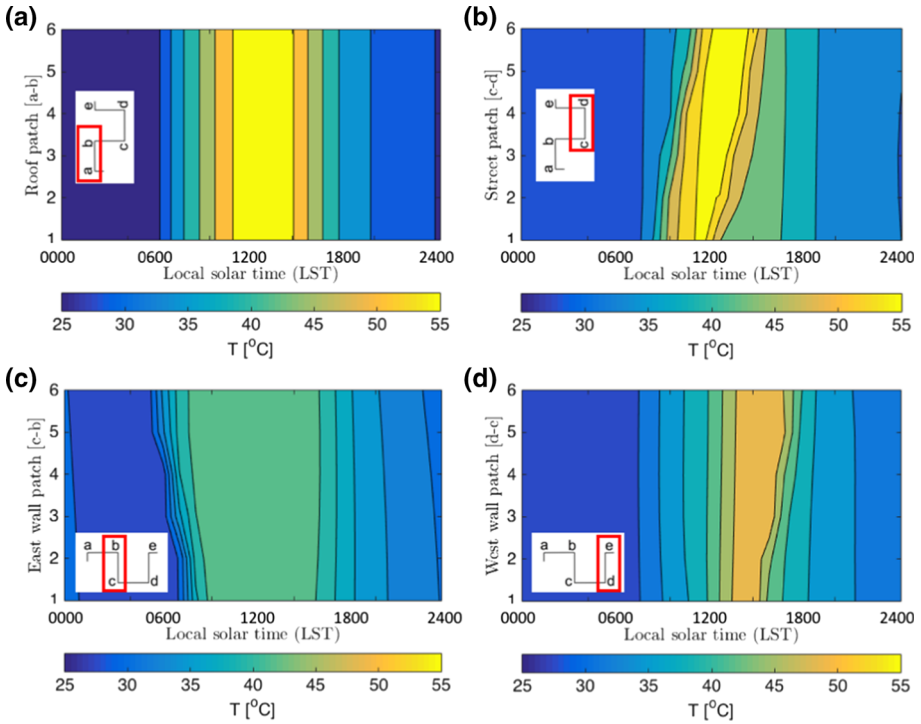
Fig. 5 Spatial facet temperatures predicted by the TUF-3D model: **a** roof, **b** street, **c** east wall, and **d** west wall. Each facet is discretized by six patches along each surface direction; facet edges **a**, **b**, **c**, **d**, and **e** according to Fig. 3

where a and b can be any two variables of interest (they are the same in case of variances). Symbols $<>$ represent spatial averaging at each vertical level. The first term on the right-hand side (I) is the flux or variance due to the mean transport, but the mean transport in the vertical direction in our simulations is zero since there is no subsidence, i.e. the mean vertical velocity $<\overline{w}> = 0$ in incompressible flow. The second term (II) is the spatial average of the time-averaged flux or variance, where a' and b' are fluctuations from the mean value at any given point in the domain. The third term (III) is the spatial average of the time-averaged quantities along different levels, also known as the dispersive fluxes or variances, where $\tilde{a}$ and $\tilde{b}$ are fluctuations from the mean values along different levels. The dispersive kinetic energy can be calculated as

$$<\tilde{k}> = \frac{1}{2}\left(<\tilde{u}_x^2> + <\tilde{u}_y^2> + <\tilde{u}_z^2>\right). \tag{18}$$

3.2.2 Results at 0400 LST

Figure 6 shows the vertical profiles of the streamwise velocity component as well as Reynolds stress and dispersive momentum flux. The velocity profiles identify one canyon vortex with its centre at the middle of the canyon height. The addition of the roughness elements decreases the velocity magnitude within the canyon (weaker vortex) and above the canyon, however it increases the magnitude of the Reynolds stress, particularly above the canyon. The composi-
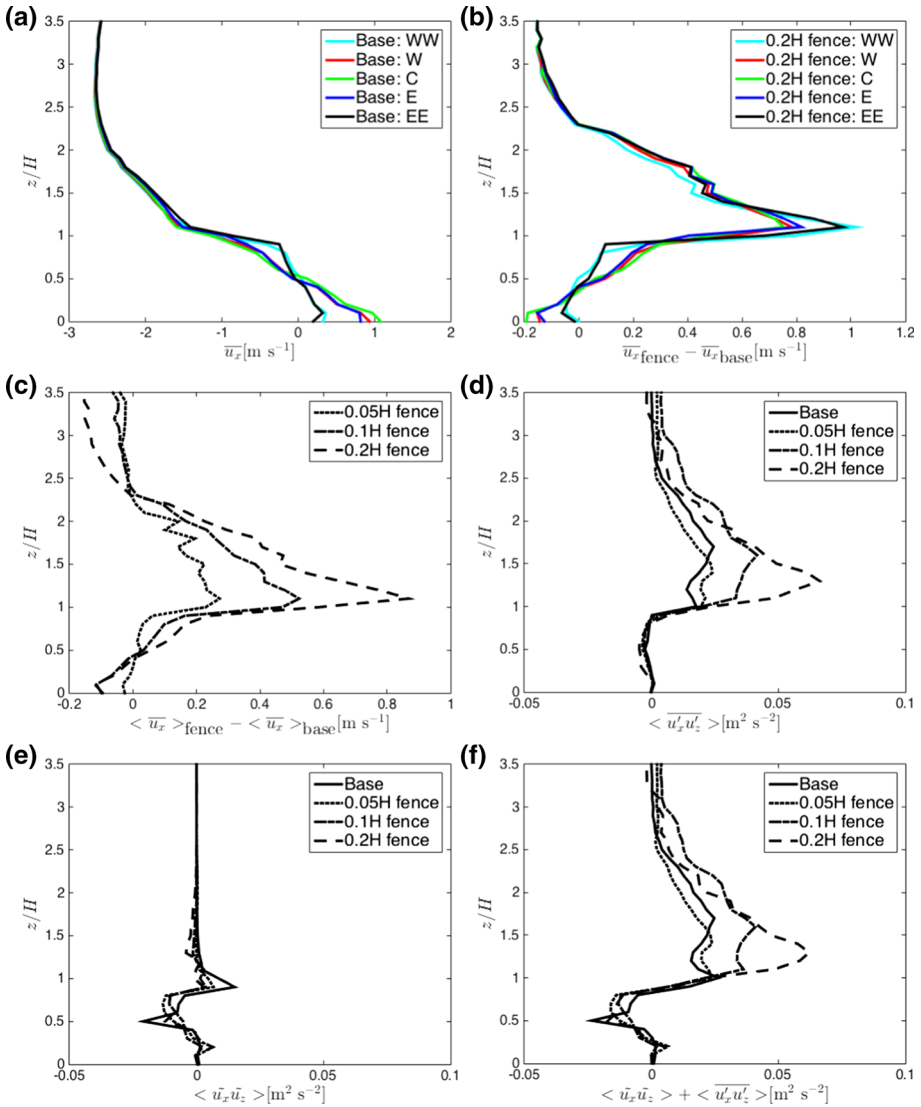
Fig. 6 Simulation results at 0400 LST; vertical profiles of **a** time-averaged streamwise velocity component at streamwise locations WW, W, C, E, and EE (see Fig. 3 for locations) for the base case; **b** change in time-averaged streamwise velocity component due to the largest roughness element; **c** change in horizontally-averaged streamwise velocity component as a result of fence implementation from $0.05H$ to $0.2H$; **d** spatial average of Reynolds stress; **e** dispersive momentum flux; and **f** total momentum flux; *Note* the forcing velocity vector is in the negative x direction

tion of the total momentum flux can be understood by comparing the Reynolds stress and the dispersive momentum flux, where above the canyon, the total momentum flux is dominated by the Reynolds stress, while within the canyon it is dominated by the dispersive momentum flux. The addition of the roughness elements does not significantly alter the dispersive momentum flux within the canyon.
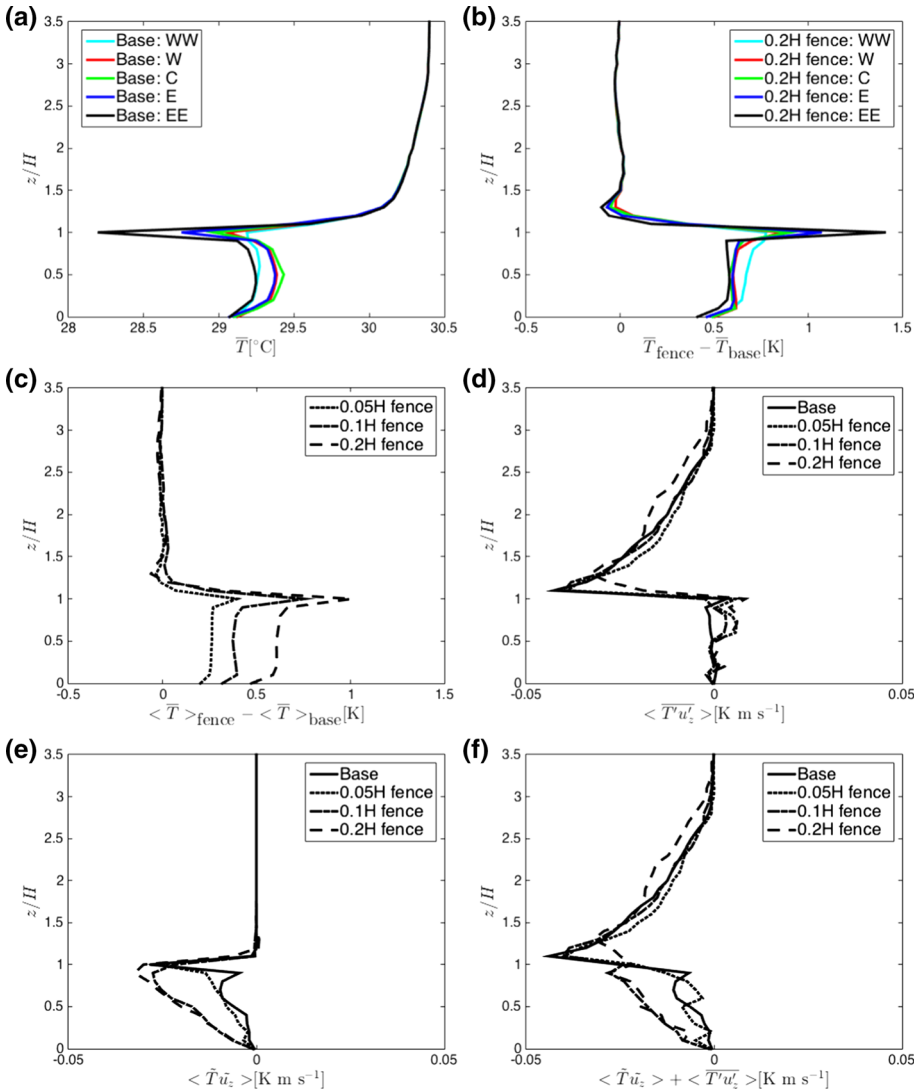
Fig. 7 Simulation results at 0400 LST; vertical profiles of **a** time-averaged temperature at streamwise locations WW, W, C, E, and EE (see Fig. 3 for locations) for the base case; **b** change in time-averaged temperature due to the largest roughness element; **c** change in horizontally-averaged temperature as a result of fence implementation from $0.05H$ to $0.2H$; **d** spatial average of turbulent heat flux; **e** dispersive heat flux; and **f** total heat flux

Figure 7 shows the vertical profiles of temperature as well as turbulent and dispersive heat fluxes. At this time (early morning) the roof is substantially colder than the canyon walls or the air aloft. The cold air in contact with the roof mixes with the canyon air due to turbulence at the roof height, resulting in the cooling of the canyon air. With the addition of the roughness elements, the mixing of this cold air with the canyon air is inhibited so that cold air is directed upwards with mixing enhanced above the canyon height. Furthermore, with increasing roughness-element height the canyon cooling due to cold air above the roof is less

and less effective. Temperature profiles inside the canyon show that above the street level there is 0.5 K heating for the largest roughness element. The total heat flux can be understood by comparing the turbulent and the dispersive heat fluxes, where the profiles of the turbulent and the dispersive heat fluxes show negative values for above and within the canyon, suggesting that heat is transported downwards by warm parcels of air (T', $\tilde{T} > 0$) transported downwards (w', $\tilde{w} < 0$) or alternatively cold parcels of air (T', $\tilde{T} < 0$) transported upwards (w', $\tilde{w} > 0$). The addition of the roughness elements creates a larger and dominant negative dispersive heat flux but a smaller and subdominant negative turbulent heat flux, resulting in the net heat transported downwards and warming of the canyon air. As a result, in this case using the roughness elements may be undesirable at this time, so if possible, the roughness elements may be deactivated, e.g. using an electric actuator.

Figure 8 shows the vertical profiles of passive scalar concentration (unitless) as well as turbulent and dispersive passive scalar fluxes. The maximum concentration is observed near the leeward wall, i.e. EE, early in the morning (0400 LST), in agreement with, e.g., Tominaga and Stathopoulos (2013). With the addition of the roughness elements, during this time the passive scalar (pollutant) concentration above the street level decreases by 2% of the street-level concentration at all streamwise locations, and a larger roughness element results in an enhanced reduction of concentration above the street level. The mechanisms responsible for this reduction can be understood by analyzing the total passive scalar concentration flux, where above the canyon the turbulent flux dominates, while within the canyon the dispersive flux dominates. Overall there is a net positive flux at all levels, which can be perceived as a net transport of pollutants upward with patches of high concentration (s', $\tilde{s} > 0$) transported upwards (w', $\tilde{w} > 0$), or alternatively patches of low concentration (s', $\tilde{s} < 0$) transported downward (w', $\tilde{w} < 0$). The addition of the roughness elements creates a positive shift in the total passive scalar concentration flux above and below the roughness elements, justifying the concentration reduction, by flushing of the canyon space to remove the pollutants. Consequently the passive scalar concentration decreases above the street level, which is desirable in this case.

Figure 9 shows the vertical profiles of turbulent and dispersive kinetic energies. The total kinetic energy is dominated by the TKE both inside and above the urban canyon, and the TKE is the highest above the urban canyon. The addition of the roughness elements increases the TKE both inside and above the canyon at all observed streamwise locations.

Figure 10 shows the distribution of mean difference between the upstream and the domain temperatures as well as the mean passive scalar concentration. In agreement with Figs. 7 and 8, it can be observed that the addition of the roof fence overall increases the temperature and decreases the passive scalar concentration in the canyon space.

3.2.3 Results at 1600 LST

Figure 11 shows the vertical profiles of the streamwise velocity component as well as Reynolds stress and dispersive momentum flux. The velocity profiles identify one canyon vortex with its centre at the middle of the canyon height. The addition of the roughness elements decreases the velocity magnitude within the canyon (weaker vortex) for modest size roughness elements (i.e. $0.05H$ or $0.1H$), but reverses the vortex rotation direction for the largest roughness element (i.e. $0.2H$). In addition, the roughness elements induce recirculation behind the fence above the canyon, which is evident from a large negative difference in the horizontally-averaged streamwise velocity component behind the roughness elements, particularly when a large roughness element is used. The roughness elements increase the magnitude of the Reynolds stress, particularly above the canyon, where the total momentum
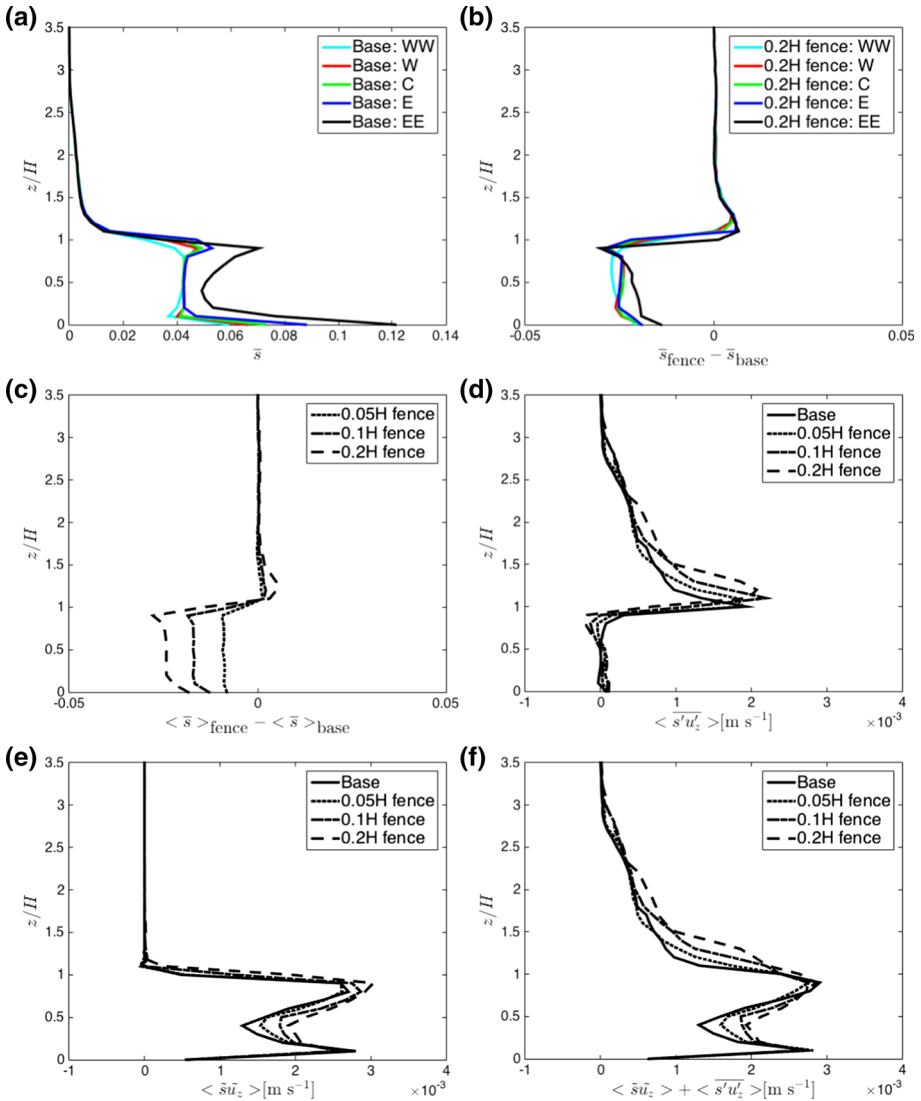
Fig. 8 Simulation results at 0400 LST; vertical profiles of **a** time-averaged passive scalar at streamwise locations WW, W, C, E, and EE (see Fig. 3 for locations) for the base case; **b** change in time-averaged passive scalar due to the largest roughness element; **c** change in horizontally-averaged passive scalar as a result of fence implementation from $0.05H$ to $0.2H$; **d** spatial average of turbulent passive scalar flux; **e** dispersive passive scalar flux; and **f** total passive scalar flux

flux is dominated by the Reynolds stress, while within the canyon the Reynolds stress and the dispersive momentum flux are comparable. The addition of the roughness elements does not significantly alter the dispersive momentum flux within the canyon except for the higher elevation just below the roof level.

Figure 12 shows the vertical profiles of temperature as well as turbulent and dispersive heat fluxes. At this time (mid afternoon) the roof is substantially warmer than other surfaces
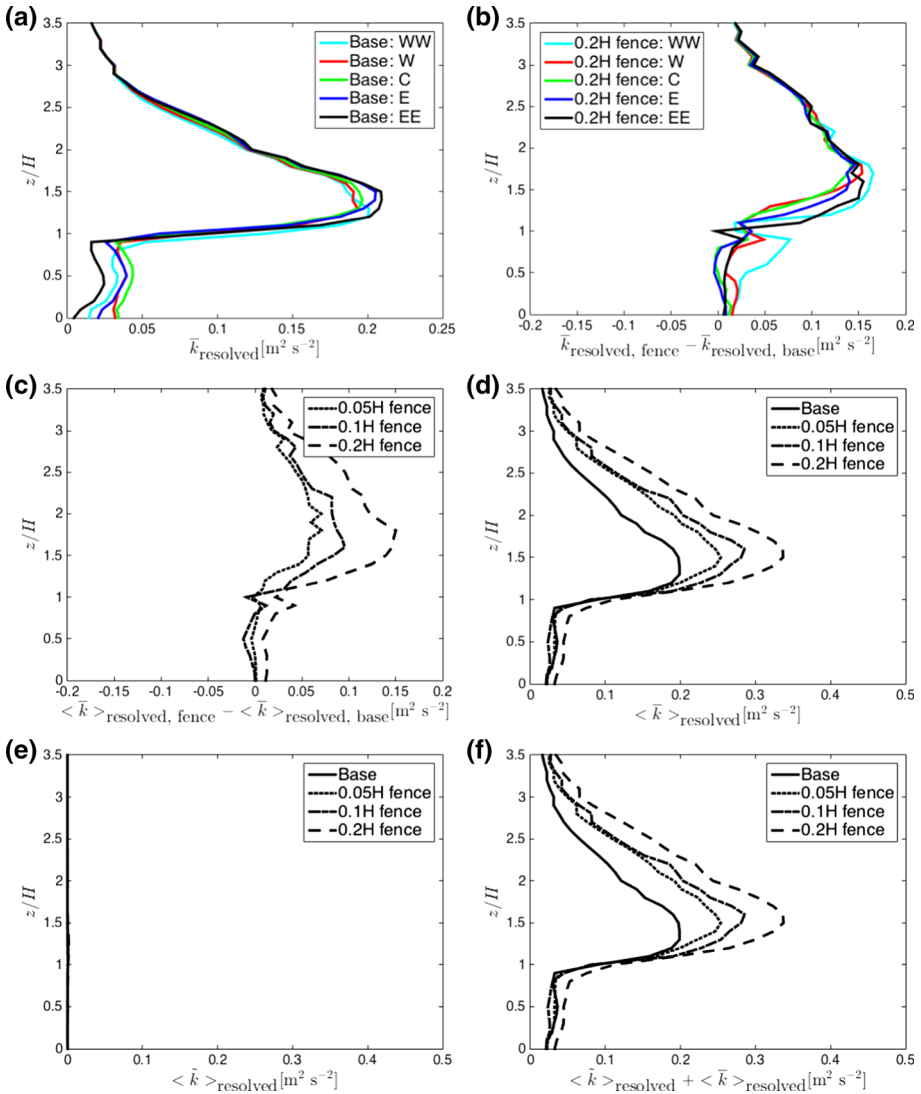
Fig. 9 Simulation results at 0400 LST; vertical profiles of **a** time-averaged TKE in the urban canyon at streamwise locations WW, W, C, E, and EE (see Fig. 3 for locations); **b** change in time-averaged TKE due to the largest roughness element; **c** change in horizontally-averaged TKE as a result of fence implementation from $0.05H$ to $0.2H$; **d** spatial average of TKE; **e** dispersive kinetic energy; and **f** total kinetic energy

or the air aloft, so the warm air in contact with the roof mixes with the canyon air due to turbulence at the roof height, resulting in the heating of the canyon air. With the addition of the roughness elements, the mixing of this warm air with the canyon air is inhibited, and warm air is directed upwards with mixing enhanced above canyon height. Furthermore, with the increasing roughness-element height the canyon heating by warm roof air is less and less effective particularly above the street level, except for elevations below the roof level near the windward wall (EE), where a local increase in the temperature is observed. Profiles of
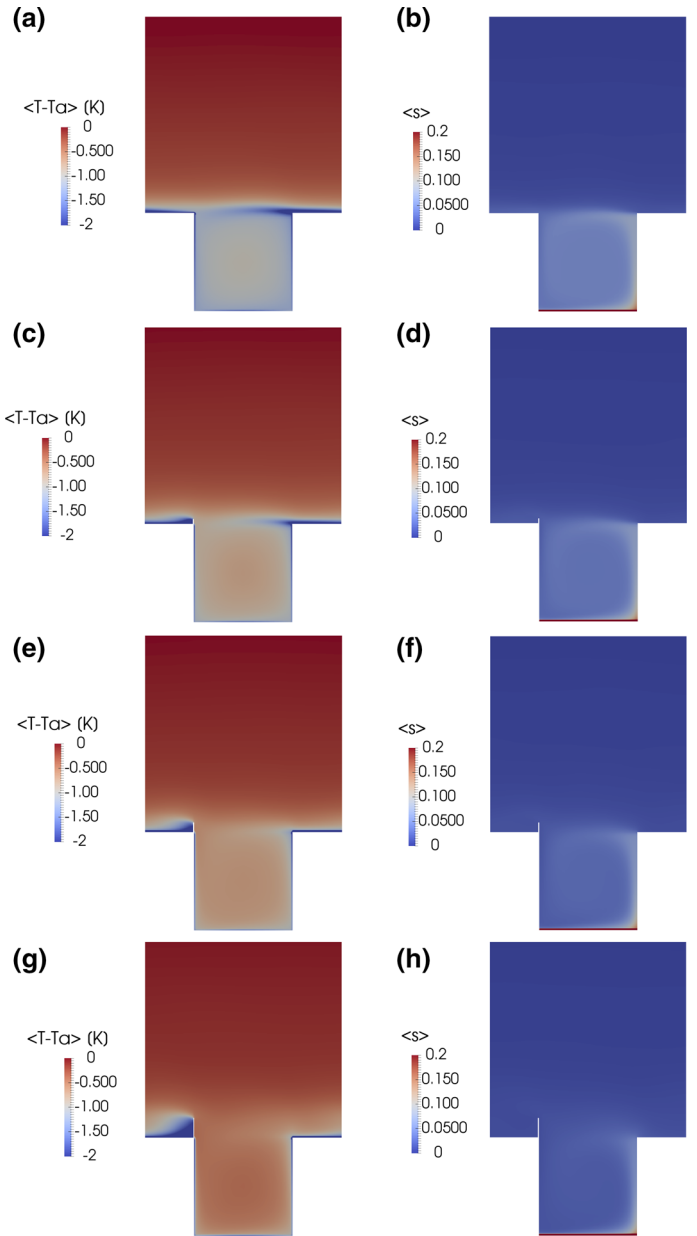
Fig. 10 Simulation results at 0400 LST; distributions of mean difference between upstream (T_a) and domain (T) temperatures (*left*) and mean passive scalar concentration (*right*) for **a**, **b** the base case; **c**, **d** 0.05H fence; **e**, **f** 0.1H fence; and **g**, **h** 0.2H fence

the temperature inside the canyon show that above the street level there is 1 K cooling for the largest roughness element. The total heat flux can be taken as the combination of the turbulent and dispersive heat fluxes, where in all cases there is a net positive total heat flux (considering all levels), suggesting that heat is transported upwards by warm parcels of air (T', $\tilde{T} > 0$)
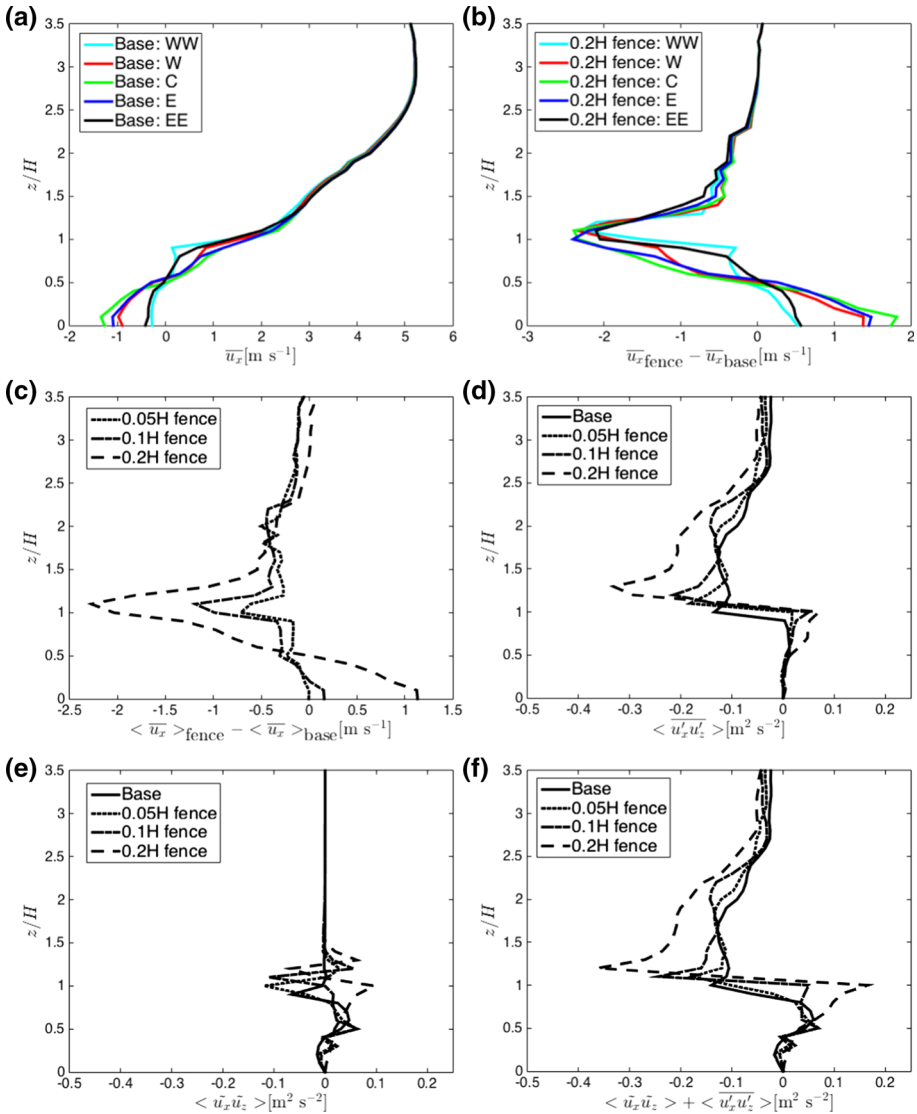
Fig. 11 Simulation results at 1600 LST; vertical profiles of **a** time-averaged streamwise velocity component at streamwise locations WW, W, C, E, and EE (see Fig. 3 for locations) for the base case; **b** change in time-averaged streamwise velocity component due to the largest roughness element; **c** change in horizontally-averaged streamwise velocity component as a result of fence implementation from $0.05H$ to $0.2H$; **d** spatial average of Reynolds stress; **e** dispersive momentum flux; and **f** total momentum flux

transported upwards (w', $\tilde{w} > 0$) or alternatively cold parcels of air (T', $\tilde{T} < 0$) transported downwards (w', $\tilde{w} < 0$). The addition of modest size roughness elements (i.e. $0.05H$ or $0.1H$) results in a small positive change of total heat flux justifying the modest reduction in the temperature above the street level, but with a large roughness element ($0.2H$), the dispersive heat flux, particularly in the lower portion of the canyon, shifts to positive values, justifying a greater temperature reduction above the street level. The lowering of canyon air
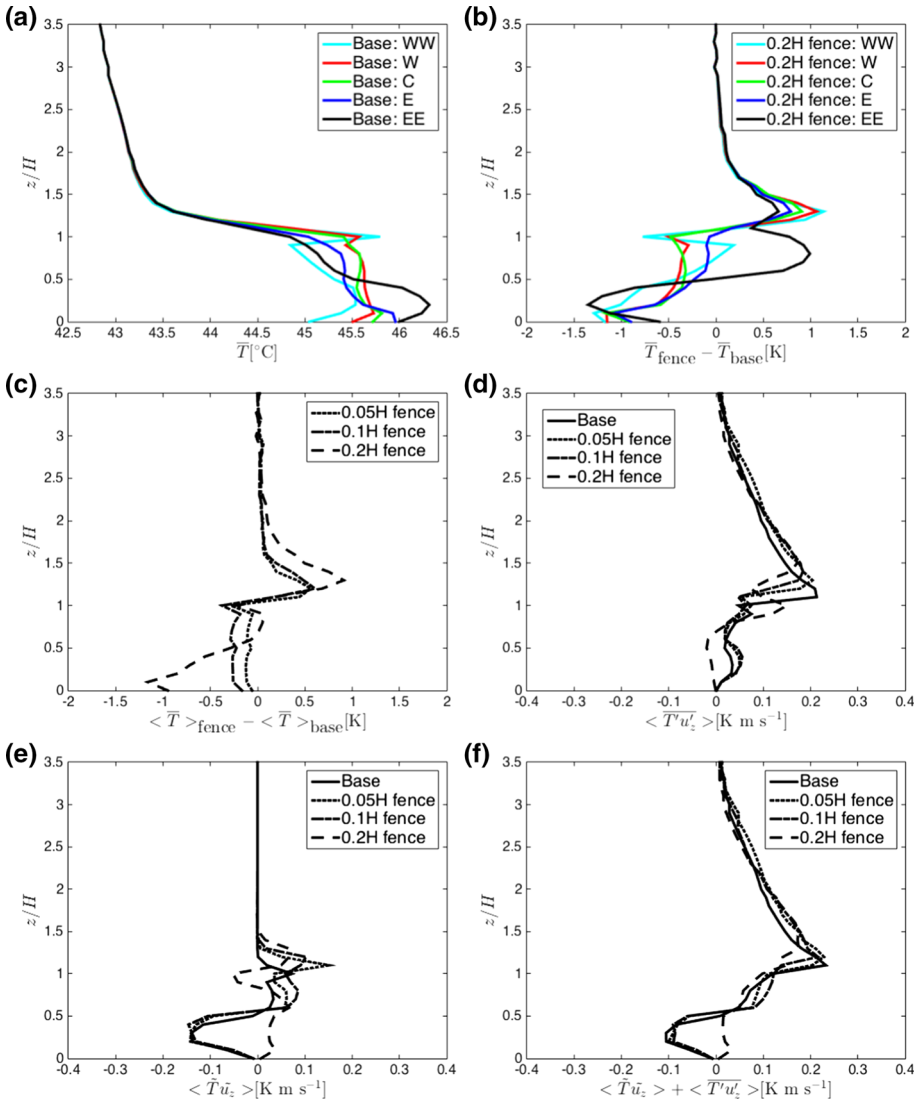
Fig. 12 Simulation results at 1600 LST; vertical profiles of **a** time-averaged temperature at streamwise locations WW, W, C, E, and EE (see Fig. 3 for locations) for the base case; **b** change in time-averaged temperature due to the largest roughness element; **c** change in horizontally-averaged temperature as a result of fence implementation from $0.05H$ to $0.2H$; **d** spatial average of turbulent heat flux; **e** dispersive heat flux; and **f** total heat flux

temperature by this mechanism is desirable, so if possible the roughness elements may be activated during this time.

Figure 13 shows the vertical profiles of passive scalar concentration as well as turbulent and dispersive passive scalar fluxes. The maximum concentration is observed near the leeward wall, i.e. WW in the afternoon (1600 LST). During this time the passive scalar (pollutant) concentration above the street level increases by 20% near the windward wall but decreases by 10% near the leeward wall, for an overall increase of 7% of the street-level concentration. The
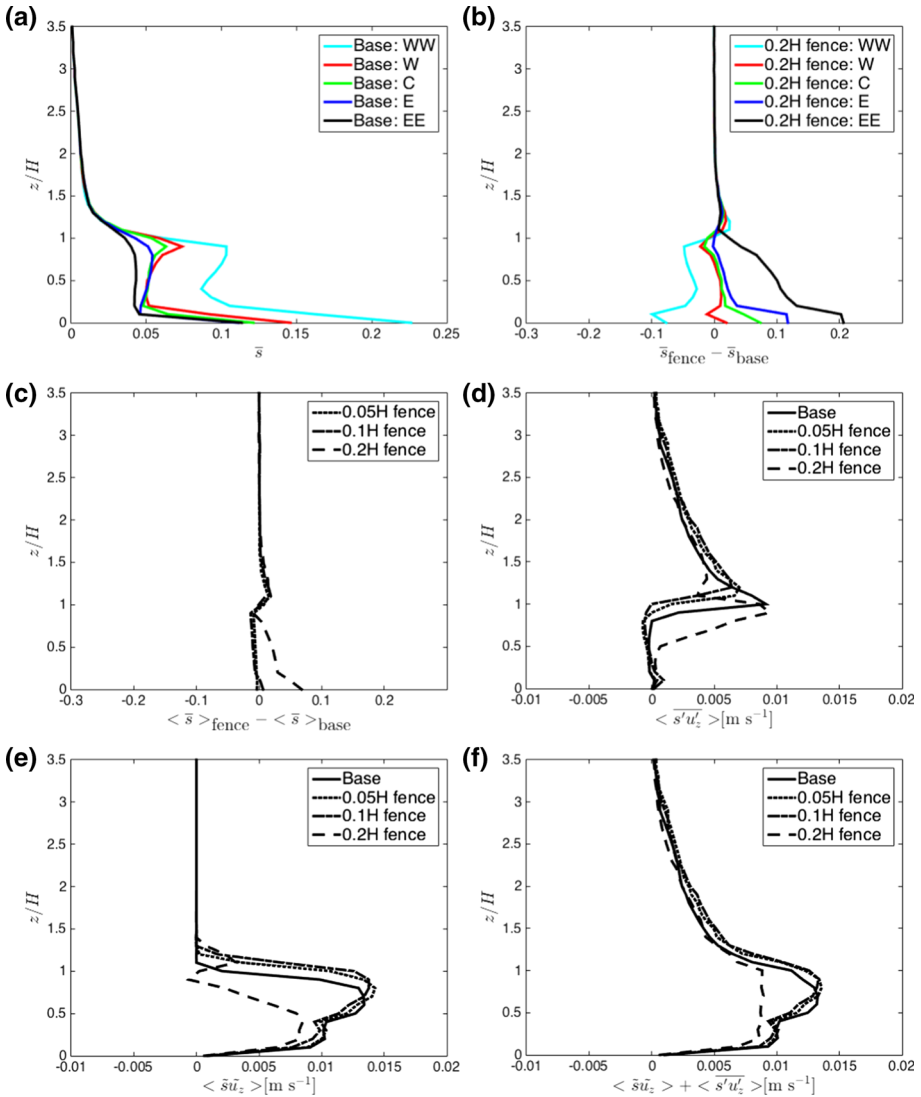
Fig. 13 Simulation results at 1600 LST; vertical profiles of **a** time-averaged passive scalar at streamwise locations WW, W, C, E, and EE (see Fig. 3 for locations) for the base case; **b** change in time-averaged passive scalar due to the largest roughness element; **c** change in horizontally-averaged passive scalar as a result of fence implementation from $0.05H$ to $0.2H$; **d** spatial average of turbulent passive scalar flux; **e** dispersive passive scalar flux; and **f** total passive scalar flux

mechanisms responsible for this increase can be understood by analyzing the total passive scalar concentration flux, where the overall flux is positive at all levels, suggesting that there is a net transport of pollutants upwards with patches of high concentration (s', $\tilde{s} > 0$) transported upwards (w', $\tilde{w} > 0$), or alternatively patches of low concentration (s', $\tilde{s} < 0$) transported downwards (w', $\tilde{w} < 0$). The addition of modest size roughness elements (i.e. $0.05H$ or $0.1H$) does not result in a significant change of the total heat flux, justifying the unaltered concentration within the canyon, but with a large roughness element ($0.2H$), the
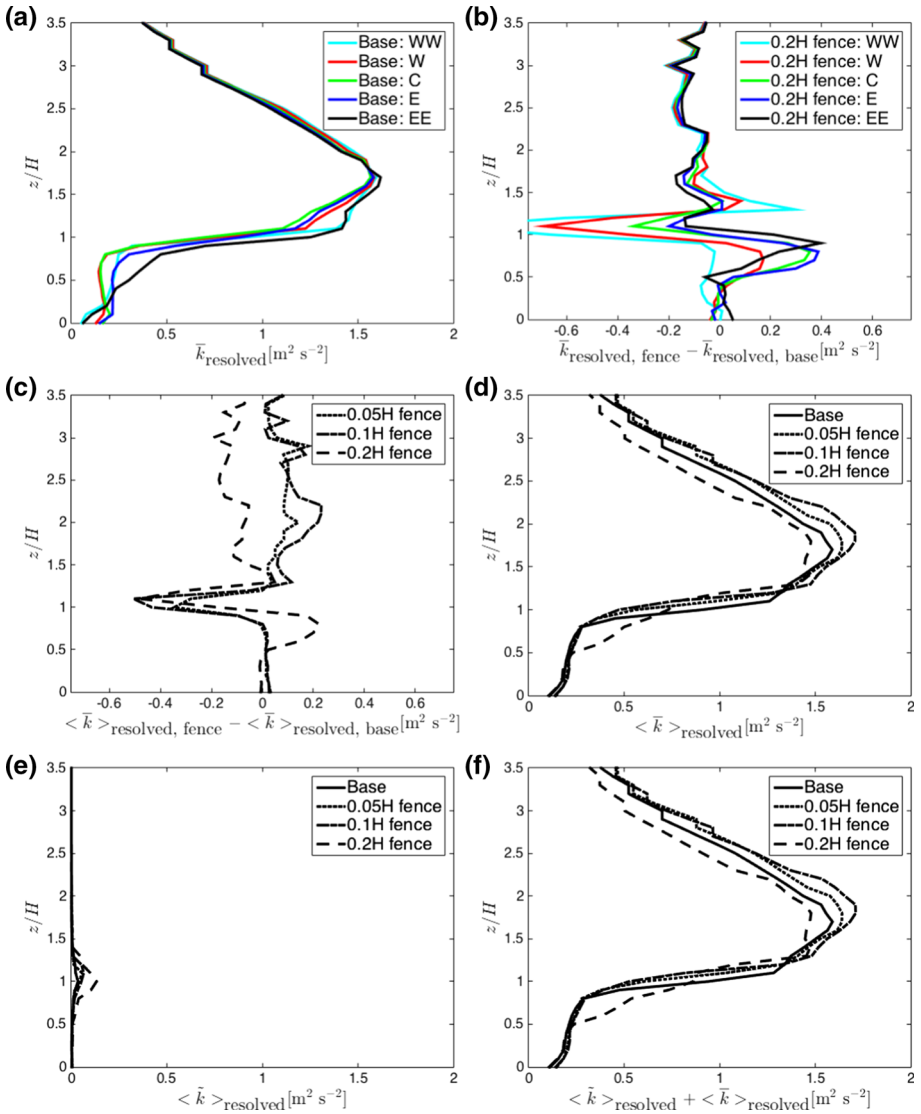
Fig. 14 Simulation results at 1600 LST; vertical profiles of **a** time-averaged TKE in the urban canyon at streamwise locations WW, W, C, E, and EE (see Fig. 3 for locations); **b** change in time-averaged TKE due to the largest roughness element; **c** change in horizontally-averaged TKE as a result of fence implementation from $0.05H$ to $0.2H$; **d** spatial average of TKE; **e** dispersive kinetic energy; and **f** total kinetic energy

dispersive heat flux reduces within the canyon, justifying an increase in concentration near the street level. Although only by 7 %, the increase of passive scalar concentration above the street level is undesirable in this case.

Figure 14 shows the vertical profiles of turbulent and dispersive kinetic energies. The total kinetic energy is dominated by the TKE both inside and above the urban canyon, and the TKE is the highest above the urban canyon. The addition of the roughness elements does not increase the TKE above the canyon, which is already high, but to the contrary reduces

it. On the other hand, the TKE is increased within the canyon, particularly below the roof level, for the largest roughness element, suggesting that the increasing TKE in the canyon is responsible for the weakening of the canyon vortex, which could be the underlying reason for the reduced temperature and the passive scalar dispersive fluxes.

Figure 15 shows the distribution of mean difference between the upstream and the domain temperatures as well as the mean passive scalar concentration. In agreement with Figs. 11, 12, and 13, it can be observed that the addition of the roof fence has a non-uniform effect on the mean temperature and passive scalar concentration within the canyon space. It can also be seen that the addition of the largest roughness element results in the reversal of the main vortex rotation direction in the canyon.

3.2.4 Reynolds Number and Richardson Number

The effect of roof-edge roughness elements on the airflow and heat transfer changes in the canyon can be further understood by calculating the building Reynolds number and the bulk Richardson number at building height given as

$$Re_H = \frac{U_H H}{\nu}, \tag{19}$$

$$Ri_b = \frac{gH}{U_H^2} \frac{T_H - T_S}{T_A}, \tag{20}$$

where subscript H denotes the building height, subscript A denotes the upstream location, and subscript S denotes the street level. Re_H and Ri_b are calculated at the centre of the canyon in the streamwise direction and are provided in Table 2. Re_H is very high and about one order of magnitude larger at 1600 LST than at 0400 LST due to higher wind speeds. The addition of the roughness elements does not appear to change Re_H dramatically, but Ri_b is very sensitive to the addition of the roughness elements. At 0400 LST, $Ri_b = 0.037$ for the base case with no roughness elements, indicating a weak thermally stable condition due to the presence of a higher temperature at the roof level in comparison to the lower temperature at the street level. The addition of the roughness elements imposes a different mixing pattern, discussed earlier, and results in warming of the canyon air and shifting of the temperature at building height towards higher values (see Fig. 7). As a result, Ri_b becomes a larger positive number as high as $Ri_b = 0.31$ for the largest roughness element. The overall effect is that the canyon air becomes more thermally stable. In contrast, at 1600 LST, Ri_b is two to four orders of magnitude smaller than the case for 0400 LST, possibly caused by very high wind speeds that result in a practically thermally neutral condition. For the base case $Ri_b = 9.2 \times 10^{-4}$, but with the implementation of the roughness elements, Ri_b becomes negative as low as $Ri_b = -1.8 \times 10^{-3}$, suggesting that the stability in canyon air is moved from a weakly thermally stable condition to a weakly thermally unstable condition. This is again supported by the fact that the observed mixing pattern, discussed earlier, results in cooling of the canyon air and shifting of the temperature at the building height toward lower values (see Fig. 12).

3.3 Limited Two-Way Coupling Tests

To address the potential errors as a result of one-way coupling of the TUF-3D and CFD models, we perform a limited two-way coupling simulation for the case when the largest roughness element ($0.2H$) is used. The differences between the one-way and two-way approaches for the mean temperature and the passive scalar concentration near the street level are analyzed.
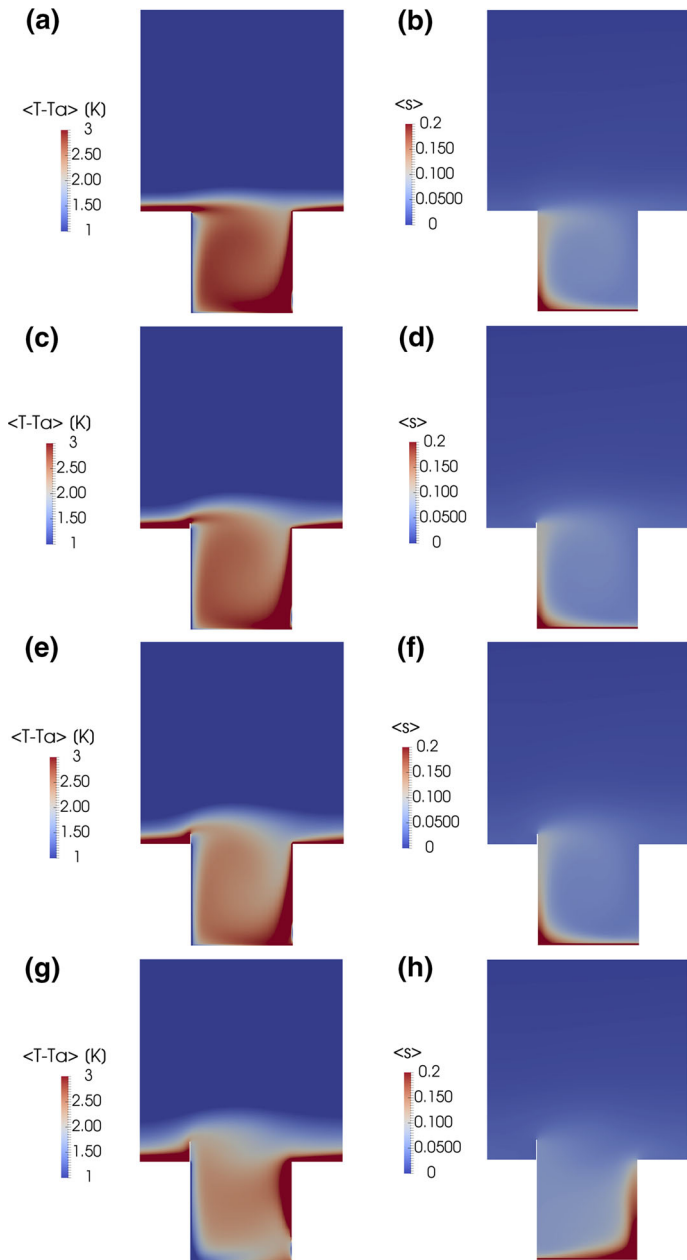
Fig. 15 Simulation results at 1600 LST; distributions of mean difference between upstream (T_a) and domain (T) temperatures (*left*) and mean passive scalar concentration (*right*) for **a**, **b** the base case; **c**, **d** $0.05H$ fence; **e**, **f** $0.1H$ fence; and **g**, **h** $0.2H$ fence

Table 2 Effect of roof roughness elements on building Reynolds and bulk Richardson numbers at 0400 LST and 1600 LST

Case	Re_H (0400 LST)	Ri_b (0400 LST)	Re_H (1600 LST)	Ri_b (1600 LST)
Base	8.3×10^5	0.037	4.6×10^6	9.2×10^{-4}
$0.05H$ fence	7.7×10^5	0.13	4.6×10^6	-3.4×10^{-5}
$0.1H$ fence	7.0×10^5	0.21	4.6×10^6	-6.5×10^{-4}
$0.2H$ fence	6.8×10^5	0.31	4.7×10^6	-1.8×10^{-3}

The two-way coupling has a minimal effect at 0400 LST when the mean temperature above the street level changes by less than 0.5 K (close to zero) and the mean passive scalar concentration at the same location only decreases by 0.003 or 0.3% of the street-level concentration. At 1600 LST, however, two-way coupling results in an additional 1 K in the temperature reduction above the street level, while the passive scalar concentration at the same location only increases by 0.019 or 1.9% of the street-level concentration. These results bolster the justification for using the roughness elements as a strategy to reduce the street-level temperatures during hot periods in the hot climate. These tests also indicate that the one-way coupling provides a more conservative estimate of the roughness elements' potential to reduce the street-level temperatures.

4 Conclusions and Future Work

The sensitivities of momentum, temperature, and passive scalar concentration (pollutant released from the street level) inside and above a two-dimensional urban canyon in hot climate were studied in response to the implementation of roof-edge roughness elements. The study was supported by meteorological measurements that were obtained from the Masdar City of Abu Dhabi in United Arab Emirates and used to force two models for the analysis. These models included the Temperature of Urban Facets (TUF-3D) energy balance model, which provided the surface temperature boundary conditions by one-way coupling to a CFD model, an LES model from OpenFOAM 3.0.1, which simulated detailed airflow, heat transfer, and passive scalar transport. A street-canyon aspect ratio of unity was considered while the roughness element height was varied from 5 to 20% of the building height (H). The simulation was performed for two local solar times (LST) during the coolest (0400 LST) and warmest (1600 LST) periods of the hottest day of the year in August 2010. The roughness elements were placed on the windward side of the roof at 0400 LST (leeward side of the roof at 1600 LST due to reversal of the wind direction).

The implementation of the roughness elements altered the airflow, heat transfer, and passive scalar transport inside and above the canyon. At 0400 LST the temperature inside the canyon and above street level increased by 0.5 K as a result of implementing the tallest roughness element, but for the same conditions at 1600 LST, this temperature decreased conservatively by 1 K. The reduction of temperature at 1600 LST by 1 K would help ameliorate outdoor thermal comfort and can potentially result in significant energy savings for conventional air conditioning systems that expel heat into the canyon air. It has been suggested that the refrigeration cycle coefficient of performance is very sensitive to temperature change at the high or low temperature reservoirs, and a reduction in the high temperature reservoir can significantly reduce work input into the refrigeration cycle, and therefore elec-

tricity consumption (Armstrong et al. 2009). Also, since there are feedback mechanisms, a lower outdoor temperature implies less cooling demand by the building and therefore less injection of waste heat from air conditioning systems. As far as passive scalar concentration (pollutant) was concerned, early in the morning and when the tallest roughness element was implemented, the pollutant concentration decreased by 2% of the street-level concentration, but for the same conditions in mid afternoon, the pollutant concentration increased by 7% of the street-level concentration. These changes can be understood as a function of time of day as well as the wind direction relative to the placement of the roughness elements, i.e. above the leeward or windward walls.

The changes in air temperature and passive scalar concentration were a combined outcome of the changes in airflow, turbulent fluxes, and dispersive fluxes. The analysis suggested that the active or passive utilization of roof roughness elements can improve thermal comfort (daytime) and air quality (nighttime) inside the canyon as well as reduce energy consumption by conventional air conditioning equipment (daytime). A sensitivity test employing a limited two-way coupling of the models indicated that the potential for reducing temperatures during the daytime can be even higher, but the reduction in street-level temperatures during daytime, however, occurs at the cost of slightly increasing the street-level pollutant concentrations.

For future work, our predictions should be validated experimentally. Our TUF-3D and LES models should also be coupled to perform two-way simulations to provide more accurate estimates of temprature reduction. This analysis should be extended to three-dimensional canyons with street intersections, higher canyon aspect ratios, more detailed seasonal and diurnal variations, and irregular urban morphology. It is also desirable to parametrize the effect of mid-range roughness elements, such as the roof fence, on vertical exchanges of momentum, energy, and atmospheric constituents for use in mesoscale models. This task should be accomplished using CFD modelling, wind-tunnel experiments, and field observations so that new one-dimensional vertical diffusion models shall be developed to better represent the complex and realistic urban morphology in mesoscale models (Aliabadi et al. 2016a, b).

Appendix 1: CFD Model Validation

A critical Reynolds number, based on the building height, of $Re_H = U_H H/\nu = 4 \times 10^3$ has been suggested for a building model to be immersed within a deep boundary layer (Castro and Robins 1977), so it is necessary to reach and exceed this Reynolds number for simulations of interest to validate our model. Validation cases are run with $Re_H = U_H H/\nu = 1.08 \times 10^4$ and a bulk Richardson number (using street-level and roof-level velocities and temperatures)

Table 3 Numerical grids for CFD validation cases

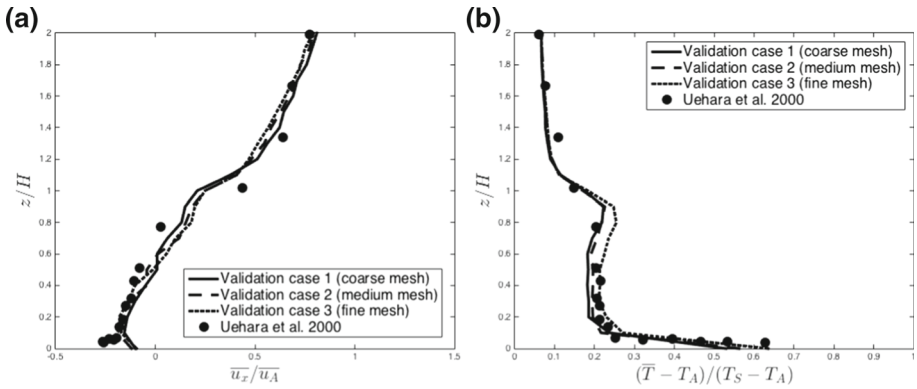| Case	Canyon $N_x - N_y - N_z$	Above canyon $N_x - N_y - N_z$	N_{Total}
1	15–12–15	15–12–36	128,520 (coarse mesh)
2	18–14–18	18–14–43	213,752 (medium mesh)
3	22–16–22	22–16–48	333,184 (fine mesh)

Fig. 16 Comparison of the LES model results with wind-tunnel experiments of Uehara et al. (2000) for **a** normalized velocity in the x direction ($\overline{u_x}/\overline{u_A}$) and **b** normalized temperature (($\overline{T} - T_A)/(T_S - T_A)$)

Table 4 Normalized mean-square error (*NMSE*) and fractional bias (*FB*) for both momentum (*M*) and energy (*E*) for comparing CFD validation cases to observations

Case	$NMSE_M$	FB_M	$NMSE_E$	FB_E
1	0.4258	−1.0319	0.0028	−0.0956
2	0.4288	−0.7956	0.0033	−0.0791
3	0.5190	−0.8612	0.0030	−0.0535

of $Ri_b = gH(T_H - T_S)/(U_H^2 T_A) = -0.35$, and the cases include multiple numerical grids according to Table 3. The model domain is as in Fig. 3 but at a 1/100 scale to match wind-tunnel experiments of Uehara et al. (2000).

These cases are compared to a wind-tunnel study (Uehara et al. 2000) of airflow over an array of blocks that are heated at the floor level (i.e. canyon street), and from this study a sub dataset with $Re_H = U_H H/\nu = 9400$ and $Ri_b = gH(T_H - T_S)/(U_H^2 T_A) = -0.21$ is used for comparison. Figure 16 shows the comparison between the LES model results and the wind-tunnel observations, where both observations and numerical model data are plotted on a vertical line in the centre of the canyon. A quantitative comparison between the wind-tunnel observations (*O*) and LES model (*M*) is also performed, using the normalized mean-square error (*NMSE*) and fractional bias (*FB*) (Hanna and Chang 2012) for both solutions: momentum (*M*), i.e. normalized velocity in the x direction, and energy (*E*), i.e. normalized temperature. These statistical metrics are quantified in Table 4 with *NMSE* and *FB* given as

$$NMSE = \frac{\sum_{i=1}^{n} (O_i - M_i)^2}{\left(\sum_{i=1}^{n} O_i\right) \left(\sum_{i=1}^{n} M_i\right)}, \tag{21}$$

$$FB = \frac{\sum_{i=1}^{n} O_i - \sum_{i=1}^{n} M_i}{0.5 \left(\sum_{i=1}^{n} O_i + \sum_{i=1}^{n} M_i\right)}. \tag{22}$$

It is confirmed that the mesh resolutions used are high enough so that the different resolutions do not affect the time-averaged solutions, and the model produces the experimental velocity and temperature fields reasonably well. The fractional bias for the momentum appears higher than expected, especially after comparing the model and observations in the figures, which is likely caused by division by a small number near zero where the momentum is close to zero at the centre of the main canyon vortex.

It must be noted that the concept of grid convergence is non-existent for LES models. In other words, a definition of a relative error may not necessarily approach zero or even reduce by further refining the numerical grid, which is the case for turbulence models that *switch* functions at a specific length scale. For example, the LES model essentially formulates and solves different sets of partial differential equations at above-grid and subgrid scales (Roache 1997). Even though grid convergence may not be verified in an LES model, a model must be run at different grid resolutions to ensure that the solution behaviour and a suitable definition of uncertainty (e.g. *NMSE* or *FB*) are bounded within a desired range.

References

Aliabadi AA, Staebler RM, de Grandpré J, Zadra A, Vaillancourt PA (2016a) Comparison of estimated atmospheric boundary layer mixing height in the Arctic and southern Great Plains under statically stable conditions: experimental and numerical aspects. Atmos-Ocean 54(1):60–74

Aliabadi AA, Staebler RM, Liu M, Herber A (2016b) Characterization and parametrization of Reynolds stress and turbulent heat flux in the stably-stratified lower Arctic troposphere using aircraft measurements. Boundary-Layer Meteorol 161(1):99–126

Armstrong PR, Jiang W, Winiarski D, Katipamula S, Norford LK (2009) Efficient low-lift cooling with radiant distribution, thermal storage, and variable-speed chiller controls-part II: annual use and energy savings. HVAC&R Res 15(2):402–432

Arnfield AJ (2003) Two decades of urban climate research: a review of turbulence, exchanges of energy and water, and the urban heat island. Int J Climatol 23(1):1–26

Balogun AA, Tomlin AS, Wood CR, Barlow JF, Belcher SE, Smalley RJ, Lingard JJN, Arnold SJ, Dobre A, Robins AG, Martin D, Shallcross DW (2010) In-street wind direction variability in the vicinity of a busy intersection in central London. Boundary-Layer Meteorol 136(3):489–513

Blackman K, Perret L, Savory E, Piquet T (2015) Field and wind tunnel modeling of an idealized street canyon flow. Atmos Environ 106:139–153

Bredberg J (2000) On the wall boundary condition for turbulence models. Internal report 00/4, Department of Thermo and Fluid Dynamics, Chalmers University of Technology, Göteborg, Sweden, 21 pp

Bueno B, Norford L, Hidalgo J, Pigeon G (2012) The urban weather generator. J Build Perf Simulat 6(4):269–281

Castro IP, Robins AG (1977) The flow around a surface-mounted cube in uniform and turbulent streams. J Fluid Mech 79(2):307–335

Cheng H, Castro IP (2002) Near wall flow over urban-like roughness. Boundary-Layer Meteorol 104(2):229–259

Christen A, Rotach MW, Vogt R (2009) The budget of turbulent kinetic energy in the urban roughness sublayer. Boundary-Layer Meteorol 131(2):193–222

Coceal O, Thomas TG, Castro IP, Belcher SE (2006) Mean flow and turbulence statistics over groups of urban-like cubical obstacles. Boundary-Layer Meteorol 121(3):491–519

Efros V (2006) Large eddy simulation of channel flow using wall functions. Thesis, Department of Thermo and Fluid Dynamics, Chalmers University of Technology, Göteborg, Sweden, 37 pp

Eliasson I, Offerle B, Grimmond CSB, Lindqvist S (2006) Wind fields and turbulence statistics in an urban street canyon. Atmos Environ 40(1):1–16

Flores F, Gerreaud R, Munoz RC (2013) CFD simulations of turbulent buoyant atmospheric flows over complex geometry: solver development in OpenFOAM. Comput Fluids 82:1–13

Giometto MG, Christen A, Meneveau C, Fang J, Krafczyk M, Parlange MB (2016) Spatial characteristics of roughness sublayer mean flow and turbulence over a realistic urban surface. Boundary-Layer Meteorol 160(3):425–452

Goodfriend E, Katopodes Chow F, Vanella M, Balaras E (2016) Large-eddy simulation of flow through an array of cubes with local grid refinement. Boundary-Layer Meteorol 159(2):285–303

Greenshields CJ (2015) OpenFOAM: The Open Source CFD Toolbox, User Guide, Version 3.0.1. Tech. rep., OpenFOAM Foundation Ltd., PO Box 56676, London, W13 3DB, UK, 230 pp

Hamdi R, Masson V (2008) Inclusion of a drag approach in the town energy balance (TEB) scheme: offline 1D evaluation in a street canyon. J Appl Meteorol Clim 47:2627–2644

Hanna S, Chang J (2012) Acceptance criteria for urban dispersion model evaluation. Meteorol Atmos Phys 116(3):133–146

Harman IN, Barlow JF, Belcher SE (2004) Scalar fluxes from urban street canyons part II: model. Boundary-Layer Meteorol 113(3):387–409

Huang Y, Hu X, Zeng N (2009) Impact of wedge-shaped roofs on airflow and pollutant dispersion inside urban street canyons. Build Environ 44(12):2335–2347

Huang YD, He WR, Kim CN (2015) Impacts of shape and height of upstream roof on airflow and pollutant dispersion inside an urban street canyon. Environ Sci Pollut R 22(3):2117–2137

Inagaki A, Kanda M (2008) Turbulent flow similarity over an array of cubes in near-neutrally stratified atmospheric flow. J Fluid Mech 615:101–120

Jayatillaka CLV (1969) The influence of Prandtl number and surface roughness on the resistance of the laminar sublayer to momentum and heat transfer. Prog Heat Mass Transfer 1:193

Kanda M, Moriwaki R, Kasamatsu F (2004) Large-eddy simulation of turbulent organized structures within and above explicitly resolved cube arrays. Boundary-Layer Meteorol 112(2):343–368

Kastner-Klein P, Berkowicz R, Britter R (2004) The influence of street architecture on flow and dispersion in street canyons. Meteorol Atmos Phys 87(1):121–131

Kim JJ, Baik JJ (2003) Effects of inflow turbulence intensity on flow and pollutant dispersion in an urban street canyon. J Wind Eng Ind Aerodyn 91(3):309–329

Klein P, Clark JV (2007) Flow variability in a North American downtown street canyon. J Appl Meteorol Clim 46:851–877

Klein PM, Galvez JM (2015) Flow and turbulence characteristics in a suburban street canyon. Environ Fluid Mech 15(2):419–438

Krayenhoff ES, Voogt JA (2007) A microscale three-dimensional urban energy balance model for studying surface temperatures. Boundary-Layer Meteorol 123(3):433–461

Krayenhoff ES, Voogt JA (2010) Impacts of urban albedo increase on local air temperature at daily-annual time scales: model results and synthesis of previous work. J Appl Meteorol Clim 49:1634–1648

Krayenhoff ES, Santiago JL, Martilli A, Christen A, Oke TR (2015) Parametrization of drag and turbulence for urban neighbourhoods with trees. Boundary-Layer Meteorol 156(2):157–189

Krpo A, Salamanca F, Martilli A, Clappier A (2010) On the impact of anthropogenic heat fluxes on the urban boundary layer: a two-dimensional numerical study. Boundary-Layer Meteorol 136(1):105–127

Kusaka H, Kondo H, Kikegawa Y, Kimura F (2001) A simple single-layer urban canopy model for atmospheric models: comparison with multi-layer and slab models. Boundary-Layer Meteorol 101(3):329–358

Launder BE, Spalding DB (1974) The numerical computation of turbulent flows. Comput Meth Appl Mech Eng 3(2):269–289

Lemonsu A, Grimmond CSB, Masson V (2004) Modeling the surface energy balance of the core of an old mediterranean city: Marseille. J Appl Meteorol 43:312–327

Li XX, Leung DYC, Liu CH, Lam KM (2008) Physical modeling of flow field inside urban street canyons. J Appl Meteorol Clim 47:2058–2067

Li XX, Britter RE, Koh TY, Norford LK, Liu CH, Entekhabi D, Leung DYC (2010) Large-eddy simulation of flow and pollutant transport in urban street canyons with ground heating. Boundary-Layer Meteorol 137(2):187–204

Li XX, Britter RE, Norford LK, Koh TY, Entekhabi D (2012) Flow and pollutant transport in urban street canyons of different aspect ratios with ground heating: large-eddy simulation. Boundary-Layer Meteorol 142(2):289–304

Louka P, Belcher SE, Harrison RG (2000) Coupling between air flow in streets and the well-developed boundary layer aloft. Atmos Environ 34(16):2613–2621

Martilli A, Santiago JL (2007) CFD simulation of airflow over a regular array of cubes. part II: analysis of spatial average properties. Boundary-Layer Meteorol 122(3):635–654

Martilli A, Clappier A, Rotach MW (2002) An urban surface exchange parameterisation for mesoscale models. Boundary-Layer Meteorol 104(2):261–304

Masson V (2000) A physically-based scheme for the urban energy budget in atmospheric models. Boundary-Layer Meteorol 94(3):357–397

Masson V, Grimmond CSB, Oke TR (2002) Evaluation of the town energy balance (TEB) scheme with direct measurements from dry districts in two cities. J Appl Meteorol 41:1011–1026

Masson V, Gomes L, Pigeon G, Liousse C, Pont V, Lagouarde JP, Voogt J, Salmond J, Oke TR, Hidalgo J, Legain D, Garrouste O, Lac C, Connan O, Briottet X, Lachérade S, Tulet P (2008) The Canopy and Aerosol Particles Interactions in TOlouse Urban Layer (CAPITOUL) experiment. Meterol Atmos Phys 102:135–157

Nakamura Y, Oke TR (1988) Wind, temperature and stability conditions in an east-west oriented urban canyon. Atmos Environ 22(12):2691–2700

Nazarian N, Kleissl J (2016) Realistic solar heating in urban areas: air exchange and street-canyon ventilation. Build Environ 95:75–93

Rafailidis S (1997) Influence of building areal density and roof shape on the wind characteristics above a town. Boundary-Layer Meteorol 85(2):255–271

Raupach MR, Thom AS, Edwards I (1980) A wind-tunnel study of turbulent flow close to regularly arrayed rough surfaces. Boundary-Layer Meteorol 18(4):373–397

Reynolds AJ (1975) The prediction of turbulent Prandtl and Schmidt numbers. Int J Heat Mass Transfer 18(9):1055–1069

Roache PJ (1997) Quantification of uncertainty in computational fluid dynamics. Annu Rev Fluid Mech 29:123–160

Rotach MW, Vogt R, Bernhofer C, Batchvarova E, Christen A, Clappier A, Feddersen B, Gryning SE, Martucci G, Mayer H, Mitev V, Oke TR, Parlow E, Richner H, Roth M, Roulet YA, Ruffieux D, Salmond JA, Schatzmann M, Voogt JA (2005) BUBBLE-an urban boundary layer meteorology project. Theor Appl Climatol 81(3):231–261

Rotta JC (1964) Temperaturverteilungen in der turbulenten grenzschicht an der ebenen Platte. Int J Heat Mass Transfer 7(2):215–228

Roulet YA, Martilli A, Rotach MW, Clappier A (2005) Validation of an urban surface exchange parameterization for mesoscale models-1D case in a street canyon. J Appl Meteorol 44:1484–1498

Saathoff P, Gupta A, Stathopoulos T, Lazure L (2009) Contamination of fresh air intakes due to downwash from a rooftop structure. J Air Waste Manag Assoc 59(3):343–353

Santiago JL, Martilli A (2010) A dynamic urban canopy parameterization for mesoscale models based on computational fluid dynamics Reynolds-averaged Navier-Stokes microscale simulations. Boundary-Layer Meteorol 137(3):417–439

Santiago JL, Martilli A, Martin F (2007) CFD simulation of airflow over a regular array of cubes. Part I: three-dimensional simulation of the flow and validation with wind-tunnel measurements. Boundary-Layer Meteorol 122(3):609–634

Santiago JL, Coceal O, Martilli A (2013) How to parametrize urban-canopy drag to reproduce wind-direction effects within the canopy. Boundary-Layer Meteorol 149(1):43–63

Santiago JL, Krayenhoff ES, Martilli A (2014) Flow simulations for simplified urban configurations with microscale distributions of surface thermal forcing. Urban Clim 9:115–133

Tabor GR, Baba-Ahmadi MH (2010) Inlet conditions for large eddy simulation: a review. Comput Fluids 39(4):553–567

Takano Y, Moonen P (2013) On the influence of roof shape on flow and dispersion in an urban street canyon. J Wind Eng Ind Aerodyn 123((Part A)):107–120

Tominaga Y, Stathopoulos T (2013) CFD simulation of near-field pollutant dispersion in the urban environment: a review of current modeling techniques. Atmos Environ 79:716–730

Uehara K, Murakami S, Oikawa S, Wakamatsu S (2000) Wind tunnel experiments on how thermal stratification affects flow in and above urban street canyons. Atmos Environ 34(10):1553–1562

van Driest ER (1956) On turbulent flow near a wall. J Aeronaut Sci 23(11):1007–1011

Vardoulakis S, Fisher BEA, Pericleous K, Gonzalez-Flesca N (2003) Modelling air quality in street canyons: a review. Atmos Environ 37(2):155–182

White FM (2003) Fluid mechanics, 5th edn. McGraw-Hill Higher Education, New York, 866 pp

Yaghoobian N, Kleissl J, Paw-U KT (2014) An improved three-dimensional simulation of the diurnally varying street-canyon flow. Boundary-Layer Meteorol 153(2):251–276

Yassin MF (2011) Impact of height and shape of building roof on air quality in urban street canyons. Atmos Environ 45(29):5220–5229

Yuan C, Ng E, Norford LK (2014) Improving air quality in high-density cities by understanding the relationship between air pollutant dispersion and urban morphologies. Build Environ 71:245–258